RSC Advances

Electroforming and Resistive Switching in Silicon Dioxide Resistive Memory Devices

Journal:	*RSC Advances*
Manuscript ID:	RA-ART-12-2014-016078.R1
Article Type:	Paper
Date Submitted by the Author:	06-Feb-2015

Complete List of Authors:	Fowler, Burt; PrivaTran, LLC, Chang, Yao-Feng; The University of Texas at Austin, Electrical and Computer Engineering; Microelectronics Research Center, Zhou, Fei; The University of Texas at Austin, Electrical and Computer Engineering Wang, Yanzhen; The University of Texas at Austin, Electrical and Computer Engineering Chen, Pai-Yu; The University of Texas at Austin, Electrical and Computer Engineering Xue, Fei; The University of Texas at Austin, Electrical and Computer Engineering Chen, Yen-Ting; The University of Texas at Austin, Electrical and Computer Engineering Bringhurst, Brad; PrivaTran, LLC, Pozder, Scott; Global Foundries, Lee, Jack; The University of Texas at Austin, Electrical and Computer Engineering

Electroforming and Resistive Switching in Silicon Dioxide Resistive Memory Devices

Burt W. Fowler,[a] Yao-Feng Chang,[b,*] Fei Zhou,[b] Yanzhen Wang,[b] Pai-Yu Chen,[b] Fei Xue,[b] Yen-Ting Chen,[b] Brad Bringhurst,[a] Scott Pozder,[c] and Jack C. Lee[b]

[a] PrivaTran, LLC, Austin, Texas 78746, USA

[b] Department of Electrical and Computer Engineering, University of Texas, Austin, Texas 78758, USA

[c] Global Foundries, Malta, New York 12020.

Abstract: Electroforming and resistive switching in SiO_2 materials are investigated by controlling anneal temperature, etch time and operating ambient. Thermal anneal in reducing ambient lowers electroforming voltage to < 10 V, providing insight into possible electroformation precursors. Conductive filaments form within ~ 4 nm of sidewall surfaces in devices with an etched SiO_2 layer, whereas most filaments are > 10 nm from the electrode edge in devices with continuous SiO_2 layers. Switching unpassivated devices fails in 1 atm air and pure O_2/N_2, with recovery of vacuum switching at ~ 4.6 V after switching attempts in O_2/N_2 and at ~ 9.5 V after switching attempts in air. Incorporating a hermetic passivation layer enables switching in 1 atm air. Discussions of defect energetics and electrochemical reactions lead to a localized switching model describing device switching dynamics. Low-frequency noise data are consistent with charge transport through electron-trapping defects. Low-resistance-state current for < 1.5 V bias is modeled by hopping conduction. A current "overshoot" phenomenon with threshold near 1.6 V is modeled as electron tunneling. Results demonstrate that SiO_2-based resistive memory devices provide a good experimental platform to study SiO_2 defects. The described electroforming methods and operating models may aid development of future SiO_2-based resistive memory products.

Key Words – silicon oxide, oxide breakdown, nonvolatile memory, resistive memory, unipolar operation, electroforming, resistive switching.

*Corresponding author: Yao-Feng Chang, email: yfchang@utexas.edu

I. Introduction

Ongoing research into resistive memory (RM) devices has resulted in many operating models for numerous device structures and materials [1-11]. Recent reports describe using SiO_2 as the active switching medium in RM devices [5, 12-14]. The long history of use in metal-oxide-semiconductor (MOS) technologies warrants further investigation of SiO_2 for potential use in high-density memory applications. Vacuum electroforming SiO_2 materials has been achieved using several device architectures, including a vertical device with an exposed sidewall etched into the SiO_2 layer [12, 15, 16], planar devices with an exposed SiO_2 surface [13], devices integrated with a nano-pillar selection diode [17], and "bulk" devices with a continuous SiO_2 layer [18]. Electrical characterization of the electroformed device demonstrates switching endurance up to 10^7 cycles [19], switching speed < 80 ns [16], and a resistance ratio approaching 10^8 under certain programing conditions [20]. Reports show that programed current is largely independent of device area and SiO_2 thickness [16, 20, 21], indicating that switching occurs in a localized region along a conductive filament (CF) [22]. Transmission electron microscopy (TEM) images show a CF comprised of disconnected Si nano-crystals ~ 3 – 5 nm in size [6, 16]. Recent *in situ* TEM studies describe a structural transition from a semi-metallic form in the low-resistance state (LRS) to a more disordered, amorphous form in the high-resistance state (HRS) [7]. More recently-reported results indicate red and green electroluminescence in the LRS and HRS, respectively [6]. Although much work has been done to characterize the SiO_2 device, many unanswered questions remain surrounding device electroforming and switching. For example, unlike most materials, SiO_2-based devices exhibit a self-compliant nature that requires no compliance current limit to program the device to the LRS. An unusual "backward-scan effect" is observed during electroforming and resistive switching (RS) that is not observed in RM devices based on other materials. In addition, only amorphous SiO_2 [16] and Si-rich SiO_x [5, 11] exhibit a unipolar current-voltage (*I-V*) response where "SET" voltage V_S is less than or equal to "RESET" voltage V_R [22], indicating that RS in silicon oxides is somewhat unique as compared to other materials. Interestingly, as the Si content increases to the point where $x < 0.8$, SiO_x-based RM devices exhibit "normal" unipolar switching characteristics where $V_S > V_R$ [11], indicating that the switching mechanisms are different in highly sub-stoichiometric devices. Another unusual characteristic of near-stoichiometric devices with x ~ 2 is that programed states in unpassivated devices are nonvolatile under 1 V constant bias at 150 °C for several hours in 1 atm air [23], but a non-oxidizing ambient such as pure N_2 or vacuum is required for RS [16, 24]. Only a few reports have studied SiO_2 electroforming in detail, with results suggesting that the Si-rich CF is formed by

oxygen reduction mechanisms [7, 16, 21, 25]. No detailed theoretical studies have investigated the microscopic, atomic-scale changes involved in electroforming, and very few reports have addressed the potential electrochemical mechanisms responsible for the unusual unipolar switching characteristics [19, 22, 25, 26].

Reported herein are electroforming, switching and charge transport results in SiO_2 RM devices using different fabrication methods, anneal treatments and operating ambients. Thermal anneal in reducing ambient lowers electroforming voltage and provides insight into possible electroformation precursors. Controlled etch studies are used to determine the physical location of the CF in devices with an exposed SiO_2 sidewall and in devices with a continuous SiO_2 layer. Low-voltage electrical stress provides an efficient method to stabilize device operation after electroforming, and data retention measurements at 100 °C indicate good potential for SiO_2 RM devices in nonvolatile memory applications. Switching is compared in 1 atm air and pure, 20% O_2 in N_2, where both ambients disable RS, but vacuum switching recovery dynamics are considerably different in devices operated in air versus those operated in O_2/N_2. Resistive switching in air is achieved by integrating a hermetic passivation layer [27]. Charge transport characteristics in LRS-devices under low bias conditions < 1.5 V are consistent with hopping mechanisms, or Mott conduction, and low-frequency noise data suggest that charge transport is through electron-trapping defects. Data fitting is used to characterize the current "overshoot" observed in LRS-devices, with results being consistent with electron tunneling phenomenon that begin to dominate the *I-V* response at moderate bias ~ 1.6 V. Discussions of SiO_2 defect energetics and electrochemical reactions lead to a model where proton exchange reactions are involved in both electroforming and RS. Energy band diagrams based on theoretical bandgaps of specific defects are consistent with state transitions in the *I-V* response, reported electroluminescence results [6], and measured electron energy barriers [26], supporting a model where electron tunneling mechanisms initiate both the SET and RESET switching transitions.

II. Device Fabrication and Test

Schematic drawings, a TEM image and secondary electron microscopy (SEM) images of the different device architectures fabricated and tested in this work are shown in Figure 1. The metal-insulator-semiconductor (MIS) devices with TaN and N+Si electrodes (Figures 1a and 1d) are simple, capacitor-like devices that have been described previously [14, 20]. The MIS device fabrication process typically includes an etch step to remove the oxide layer from the field regions surrounding the top electrode, thereby forming an SiO_2 sidewall (or edge) as

labeled in Figure 1. The MIS devices with an etched SiO_2 layer are referred to as MIS-edge devices. The metal-insulator-metal (MIM) crossbar devices (Figures 1b and 1e) used a planarized TiW lower electrode formed using chemical-mechanical planarization (CMP) with Si_3N_4 polish stop layer. A 60 nm-thick SiO_2 layer was deposited by plasma-enhanced chemical vapor deposition (PECVD), followed by 350 °C, 30-minute N_2 anneal. Via openings in the SiO_2 layer were patterned using photolithography and buffered oxide etch (BOE). A top electrode of 120 nm TiW and 900 nm Al was sputter-deposited, patterned and etched using standard wet etchants. A fourth photolithography module formed a sidewall in the SiO_2 layer between the two electrodes with BOE. Bulk devices (Figures 1c and 1f) were fabricated using a lift-off process to form the top electrode without BOE so that a continuous SiO_2 layer remained in the device [18, 27]. In these MIS-bulk devices, the SiO_2 layer was deposited using electron-beam evaporation, followed by photoresist spin-coating and photolithography to open regions in the photoresist. Metal deposition onto the exposed SiO_2 regions was then done by either sputtering or electron-beam evaporation, followed by photoresist removal to lift-off the metal in field regions and form the electrodes. As described in recent work [27], at this point in the fabrication sequence MIS-bulk devices are electroformed in vacuum followed by SU8 spin-coat and cure to provide a hermetic passivation layer that enables device operation in air, which is a key milestone helping to demonstrate the commercial viability of SiO_2 RM. Rapid thermal anneal (RTA) was done in an AG Associates Heatpulse 610 RTA. A Lake Shore Cryotronics vacuum probe chamber (< 1 mTorr) and Agilent B1500A device analyzer were used to electroform devices and measure DC *I-V* response, and a model DSO90254A digital oscilloscope was used to store data during low-frequency noise measurements.

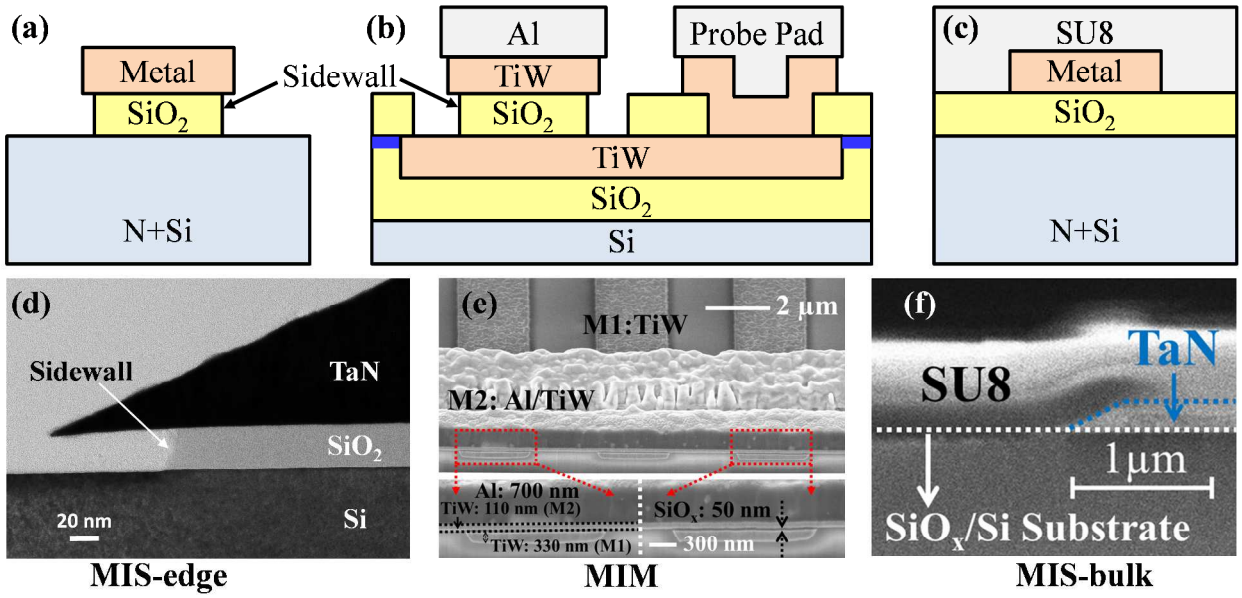

Figure 1. Cross-section schematics of three RM device architectures used to investigate electroforming and RS in amorphous SiO_2 materials: (a) MIS-edge device with exposed SiO_2 sidewall; (b) TiW MIM crossbar with exposed sidewall; (c) Passivated MIS-bulk device with continuous SiO_2 layer; (d) TEM cross section of MIS-edge device; (e) SEM top-down (upper) and cross-section (lower) images of TiW MIM device; and (f) SEM cross-section of passivated MIS-bulk device.

III. Experimental Results

Electroforming results are first presented for the three device structures shown in Figure 1, followed by a controlled etch study that identifies the location of the CF in devices with and without a SiO_2 sidewall. An efficient post-electroforming conditioning method and data retention thermal stress measurements are presented and discussed. Ambient effects on device switching are presented, followed by low-frequency noise measurements that suggest charge transport through electron-trapping defects.

III.A. Electroforming

Electroforming is the critical process determining the switching properties and operating characteristics of RM devices [8]. One SiO_2 electroforming method is to apply a forward voltage sweep until current fluctuations of 1 – 10 µA are induced, followed by a reverse sweep to 0 V (Figure 2a). Achieving current fluctuations of at least 1 µA is a clear indication that a device will successfully electroform [16, 25]. Electroforming voltage V_{EF} is defined as the

voltage where current first reaches 1 μA. Oxide breakdown (BD) in MOS devices is also associated with current fluctuations of ~1 μA [28, 29]. As discussed further in the modeling sections, this suggests that electroforming may be initiated by similar BD events. During the reverse sweep, negative differential resistance is observed where current increases with decreasing bias until a LRS is established with 10 – 100 μA typically being measured at 1 V. This "backward-scan effect" typically occurs at ~ 5 – 7 V during the reverse voltage sweep and signifies a SET transition to the LRS. This effect can also occur during RS and represents an unusual characteristic of SiO_2 that is not present in other RM materials [7, 18]. As discussed further below, the voltage dependencies of the SET and RESET transitions may lead to the backward scan effect. Electroforming requires no current compliance limit and is a one-time event after which the device operates as a reversible resistive switch.

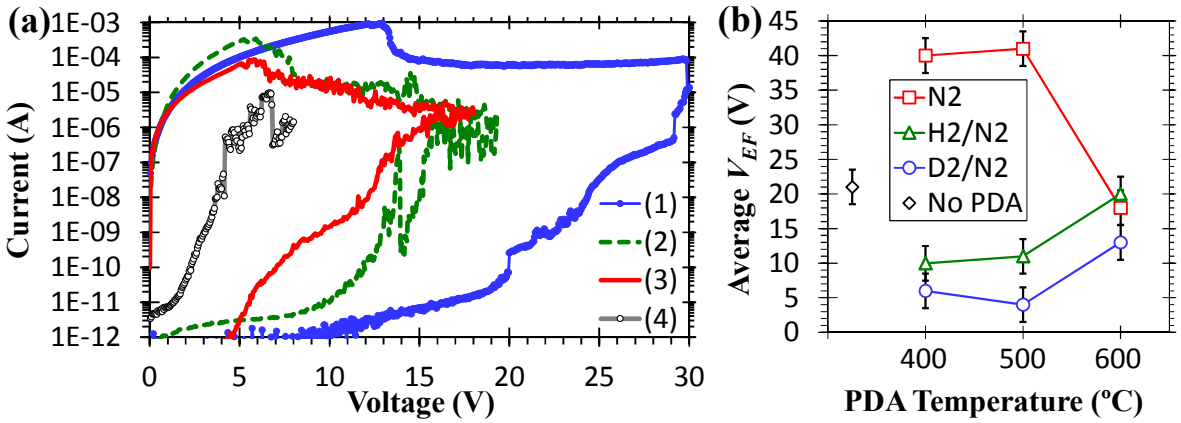

Figure 2. Electroforming results for devices having a sidewall edge. (a) Electroforming sweeps for 4 devices with SiO_2 materials deposited using: (1) thermal oxidation (30 nm); (2) e-beam evaporation (47 nm); (3) PECVD (60 nm); and (4) e-beam (51 nm) with 5-minute, 500 °C RTA in 4% D_2/N_2. (b) Average electroforming voltage V_{EF} versus PDA temperature and ambient for 5-minute RTA of ten Al / 50 nm e-beam SiO_2 / N^+Si devices at each condition with ± 3 V standard deviation bars.

The V_{EF} is strongly dependent on SiO_2 deposition methods with thermal oxide requiring high V_{EF} ~ 30 V (Figure 2a, #1), most likely due to its high-temperature growth process that produces a high-quality layer with low defect density. As a result of the low as-deposited defect density, high electric fields ~ 1 V/nm, equivalent to 10 MV/cm, are needed to increase defect levels above a critical threshold for electroforming. Lower V_{EF} ~ 15 – 20 V is needed

for materials deposited at lower temperature including physical vapor deposition [24, 30], e-beam evaporation (Figure 2a, #2), and PECVD (Figure 2a, #3). Low-temperature oxides are typically rather porous and susceptible to moisture uptake when unpassivated and exposed to air [31-36], thus making it necessary to consider H_2O-related defects as part of any investigation into potential electroforming and RS mechanisms, as discussed further below. Thermal anneal in 4% H_2 or D_2 in N_2 reduces V_{EF} to < 10 V in e-beam oxide (Figure 2a, #4). Possible reasons explaining why H_2 and D_2 anneal lowers V_{EF} are discussed below. Under certain oxide deposition and fabrication process conditions, devices can even be "auto-formed" where RS capability is observed immediately after fabrication so that a separate electroforming process is not required [22]. The detailed mechanisms responsible for auto-forming are still under investigation and will be described in future reports.

Anneal ambient and temperature effects on V_{EF} are shown in Figure 2b. As compared to $V_{EF} = 21 \pm 3$ V in control devices with no post-deposition anneal (PDA), anneal in pure N_2 at 400 °C and 500 °C increased V_{EF} by nearly 100% to ~ 40 V, presumably due to densification of the SiO_2 layer and removal of electron traps and other electrically-active defects [37]. The lowest V_{EF} values of < 10 V were found in the range of 400 – 500 degrees C for PDA in D_2/N_2 and H_2/N_2 ambients, representing a decrease of over 50% as compared to the control. The convergence of data at 600 °C is not fully understood, although it must be noted that 600 °C is above the typical anneal temperature for devices with Al electrodes, where grain growth and hillock formation in the Al can occur [38]. The values of V_{EF} ~ 18 V for 600 °C anneal are, however, consistent with reported values for devices with similar SiO_2 thickness after 10-minute, 600 °C vacuum (140 mTorr) anneal, where the decrease in V_{EF} as a result of the anneal was attributed to an increase in conduction, most likely due to higher defect levels near the oxide sidewall surface [16].

Using a "forming gas" reducing anneal to electrically passivate SiO_2 materials and their interfaces is common industry practice where typical furnace anneal process settings are 30 minutes at 350 – 450 °C in 10% H_2/N_2 [39-41]. This terminates structural defects such as Si dangling bonds and oxygen vacancies with H to form SiH and $(SiH)_2$, respectively [42, 43]. While prolonged anneal time can increase SiO_2 density by promoting Si-O cross linkage [37], the short 5-minute RTA used here should effectively terminate as-deposited defects with H without significant densification of the SiO_2 layer. This experiment was part of a larger study comparing effects on V_{EF} by PDA and a post-metalization anneal (PMA) done after sidewall etch, where it was found that both PDA and PMA in H_2 (or D_2) effectively reduced V_{EF} but that PDA had a stronger effect [25]. These results are interpreted as meaning

that PDA is more effective at passivating the as-deposited defects with H and preserving the defects throughout the remainder of the fabrication process. The substantially lower V_{EF} when using reducing anneal (Figure 2) clearly indicates that less energy is required to electroform the device and points directly to the SiH and $(SiH)_2$ defects as potential electroformation precursors.

Vacuum electroforming most devices requires an exposed sidewall or surface in the SiO_2 layer [12, 15, 16], although recent work demonstrates that electroforming is possible in some device types having a continuous SiO_2 layer [18, 27]. Figure 3 shows an electroforming *I-V* plot for a "MIS-bulk" device formed within a continuous SiO_2 layer (Figure 1c). In general, bulk device electroforming has lower yield and requires higher V_{EF} as compared to devices with an exposed sidewall [18]. Anneal of bulk devices in H_2 or D_2 is found to decrease V_{EF} by ~ 8% [18], not as large as the ~ 50% decrease observed in sidewall devices (Figure 2). Also, H_2 and D_2 anneal of bulk devices both improve electroforming yield and stabilize switching performance [18]. At this point in time, the only fabrication approach yielding working bulk devices uses a lift-off process to fabricate the top electrode, and the only oxide material successfully used in bulk devices is e-beam-deposited SiO_2. In the lift-off process, photoresist is patterned to form openings that expose the SiO_2 layer to the developer chemical and de-ionized H_2O rinse prior to metal deposition and photoresist removal. The high porosity of the e-beam material and additional H_2O exposure during the lift-off process may be important reasons why the combination of lift-off process and e-beam material successfully yields working bulk devices. As discussed further below, the lower density of e-beam SiO_2 may allow any O^{2-} ions generated during the electroforming process to readily diffuse away from the filament or drift to an electrode where the ions can react and be neutralized. In addition, porous e-beam SiO_2 may have a high density of "pinholes," which are thread-like, low-density structural defects known to increase oxide leakage current [44]. In this case the pinhole (or other defective region) with the highest initial leakage current will lead to CF formation in bulk devices. Furthermore, metal electrode deposition in the lift-off process is done at low temperature (to protect the photoresist) after exposure of the SiO_2 layer to H_2O during photoresist development, the combination of which is likely to result in a large amount of OH and other H_2O-related defects at the metal/SiO_2 interface [34, 45-53]. Pinhole defects may act similar to a surface where H_2O, OH or atomic H can diffuse deep into the SiO_2 layer, thus providing a source of reactive species during electroforming that lead directly to the defects responsible for RS.

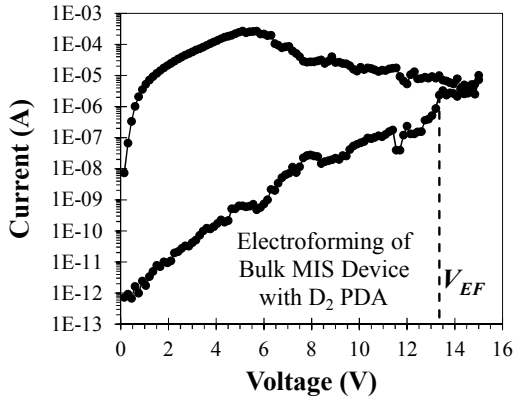

Figure 3. Bulk device electroforming *I-V* plot for a TaN/e-beam oxide (51 nm)/N+Si MIS-bulk device with 5-minute, 500 °C RTA in 4% D_2/N_2. Dashed line marks V_{EF} = 13.4 V.

Controlled etch studies were used to identify the physical location of the CF. A collection of un-passivated devices having both MIS-edge and MIS-bulk architectures (Figure 1) were first electroformed and operated in vacuum for multiple switching cycles. One-half of each device type were programed to the LRS and one-half to the HRS. Device SiO_2 layers were then etched at a rate of ~ 0.2 nm/sec in dilute HF (1:100 HF:H_2O) for various etch times and device state was measured after each etch step. A device state change indicated that the CF was attacked by the etchant, providing an estimate of the lateral depth into the SiO_2 layer where the CF was located. Figure 4 shows experimental results for 10 bulk devices and 10 sidewall devices. Most CFs in bulk devices are located more than 10 nm from the electrode edge since only one of the bulk devices was attacked by etching to a depth of 5 nm. In contrast, all CFs are within 10 nm of the sidewall with ~ 50% located within ~ 4 nm of the original sidewall surface in devices with an etched sidewall.

As discussed in more detail below, these findings support the view that O_2 and H_2O are in the immediate vicinity of the CF whenever un-passivated devices are exposed to an air environment. The findings that only low-density, porous SiO_2 materials support electroforming in bulk devices, the propensity for devices with an exposed sidewall edge to readily electroform, and the Figure 4 results showing that the CF forms very near the sidewall edge in sidewall devices clearly support the argument that water-related and hydrogen-complexed defects must be considered in any meaningful investigation into SiO_2 electroforming and RS.

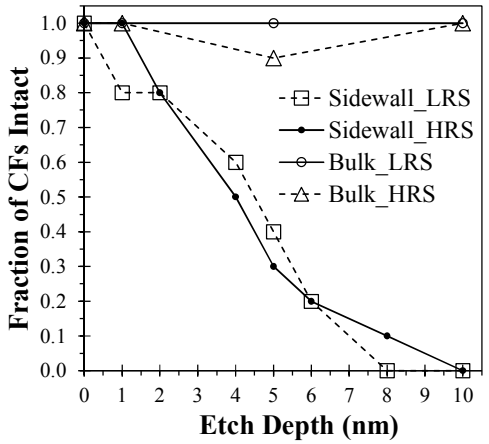

Figure 4. Fraction of CFs remaining intact after dilute HF etch to various depths.

Immediately after the electroforming process, LRS current is typically observed to increase when the device is continuously cycled between LRS and HRS. For example, Figure 5a shows that LRS current measured at 0.2 V increases as the number of voltage sweeps to 2 V increases, eventually reaching a saturation level after about 40 – 50 sweeps. This implies that the device may require 40 – 50 programing cycles in order for the LRS current to stabilize, but such extended conditioning cycles would not be desirable in a manufacturing setting. To investigate methods to reduce or eliminate the need for such conditioning cycles, room-temperature constant-voltage stress testing was done on MIM devices immediately after electroforming (Figure 5b). In these tests, voltage V_{Stress} was applied for 1000 seconds and device current was measured after each second by applying a 2 V, 100 μs pulse. For V_{Stress} = 1.75 V, the current continues to increase over a time scale of 100s of seconds, indicating that the device resistance was not stable during the test. As V_{Stress} increased, device current increased more quickly towards the saturation current of ~ 4 mA. For V_{Stress} = 3 V, the current saturates almost immediately after V_{Stress} is applied, thus indicating that constant voltage stress at 3 V provides a fast and efficient conditioning process to achieve a fully-saturated, electrically-robust CF in the LRS. Data retention of MIM devices was measured at 100 °C for 3,500 seconds (Figure 5c), where programed states were stable in the LRS and in multiple HRS conditions. Figure 5c also demonstrates the "stop voltage effect" where read current at 0.2 V progressively reduces as RESET stop voltage (SV) increases from 6 to 12 V. The efficient conditioning process and robust retention data are encouraging results

regarding potential use of SiO_2-based RM in future nonvolatile memory applications.

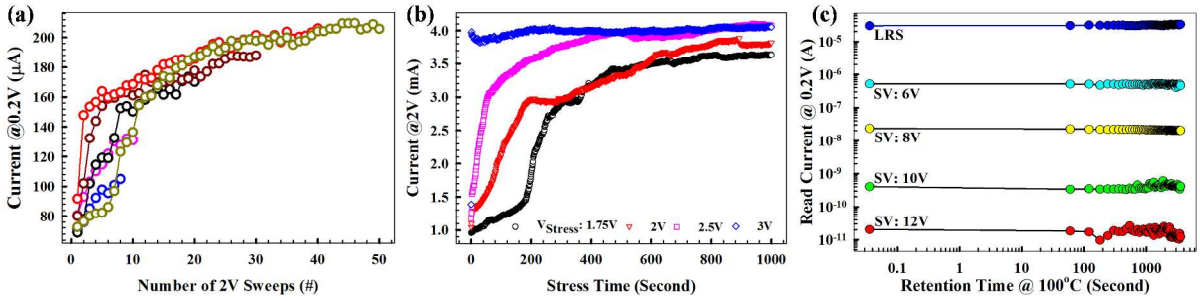

Figure 5. MIM device states in vacuum: (a) six different devices measured at 0.2 V after a series of sweeps to 2 V; (b) four devices with current measured periodically at 2 V throughout a 1000-second stress time as a function of stress voltage V_{Stress}; and (c) current measured at 0.2 V during 100 °C thermal stress for five devices programed to the LRS and several intermediate states using different stop voltage (SV).

III.B. Resistive switching

In this section the unipolar switching characteristics of SiO_2 RM devices are briefly reviewed, the stop voltage effect is investigated and the results of operating devices at 1 atm pressure in air versus pure O_2/N_2 are compared. Many different electrode materials and SiO_2 deposition methods have successfully been used to achieve RS in the three device architectures shown above in Figure 1, and many detailed switching characterization results have been previously reported [14, 18, 20, 22-24, 26].

III.B.1 Switching Characteristics

The switching *I-V* plots in Figure 6 show that devices are programed using a single voltage polarity (unipolar operation) with a 3.2 V forward/reverse sweep used to SET the device in Figure 6a to a LRS, and a 4.5 V forward sweep to RESET the device to a HRS. The HRS/LRS resistance ratio for this device is ~ 10^5 based on the measured HRS and LRS resistances at 1 V. During the SET forward/reverse sweep, the transition from HRS to LRS occurs at V_S = 2.60 V. The SET sweep continues to 3.2 V, and the LRS is clearly observed during the reverse portion of the sweep back to 0 V. It may be noted that a forward/reverse voltage sweep is not required to SET the device, as shown by the forward SET sweep in Figure 6b. In fact, a voltage pulse with magnitude V_{PULSE} can be used to SET the

device as long as $V_S < V_{PULSE} < V_R$. The RESET voltage can be either a pulse or a forward sweep. In both cases, after the maximum voltage is applied, the RESET voltage waveform must have a fast transition to 0 V so that the device will remain in a HRS. For example, if a forward/reverse voltage sweep is applied where the reverse portion of the sweep to 0 V is not sufficiently fast, the device will transition to the LRS and the RESET programing event will be unsuccessful. This phenomenon is referred to as the "backward-scan effect," and has been investigated in detail in previous reports [18].

The V_S and V_R switching transitions depend on device materials, programing voltages and the series resistance in the test circuit. The programing window, defined as $V_R - V_S$, increases with increasing series resistance [22, 54], and is $V_R - V_S = 4 - 2.6$ V = 1.4 V for the MIM sidewall device in Figure 6a. The series resistance R_S in this device was 235 Ω as determined by the resistance of the TiW trace connecting the lower electrode in the crossbar architecture (Figure 1b), which had measured sheet resistance of 1.835 Ω/square and contained 125.2 squares, and the Al/TiW trace connecting the top electrode with 0.12 Ω/square sheet resistance and 43.2 squares. RESET current I_R is often the maximum current measured from the *I-V* curve. In Figure 6a, the voltage drop across R_S is $I_R \times R_S = 0.0054$ A × 235 Ω = 1.27 V, meaning that the actual RESET voltage V_R' across the CF is $V_R' = V_R - I_R \times R_S = 2.73$ V, which is very near the SET voltage of $V_S = 2.6$ V so that $V_R' \approx V_S$. This demonstrates how R_S can be designed to provide the desired programing window.

Bulk devices electroformed in vacuum (Figure 3a) can be passivated with a hermetic, epoxy-based SU8 photoresist (Figure 1c) to achieve operation in 1 atm air, as shown in Figure 6b, although neither passivated bulk nor sidewall devices have yet been electroformed in air using existing methods [27]. The electrode in this device was covered entirely by the SU8 passivation, and a probe needle was inserted through the SU8 layer to contact the electrode during electrical test. The MIS-bulk device in Figure 6b is SET using a 4.5 V forward sweep and RESET by an 8 V sweep, and has a resistance ratio of ~ 10^7, substantially larger than the MIM sidewall device as a result of the higher RESET voltage of 8 V.

The RESET voltage sweep to 8 V shown in Figure 6b illustrates that large fluctuations are often observed for applied voltages > V_R (~ 5 V in this device). The voltage in this region of the *I-V* response is large enough so that both SET and RESET transitions can occur, leading directly to large variations in current. However, it is clear that the RESET mechanism dominates over the SET mechanism since the programed device resistance increases as RESET voltage increases, which is the so-called "stop voltage effect" as described below.

Although the switching characteristics of the two devices in Figure 6 are similar, there are several notable differences: the LRS current at 1 V of the bulk device is almost 100 times smaller than that of the sidewall device; the SET transition at V_S is stepped in the bulk device whereas it is very sharp in the sidewall device; and the programing window is considerably larger in the bulk device (2.4 V) as compared to the sidewall device (1.4 V). These differences are attributed to a more tenuous CF and overall higher R_S in the bulk device. As described in more detail in a recent report [22], more O^{2-} ions may be able to escape into the vacuum when electroforming sidewall devices, whereas bulk oxide layers may trap more O^{2-} ions within the SiO_2 layer that re-oxidize portions of the CF as it is being formed, thus resulting in larger V_{EF} and higher internal filament resistance in bulk devices.

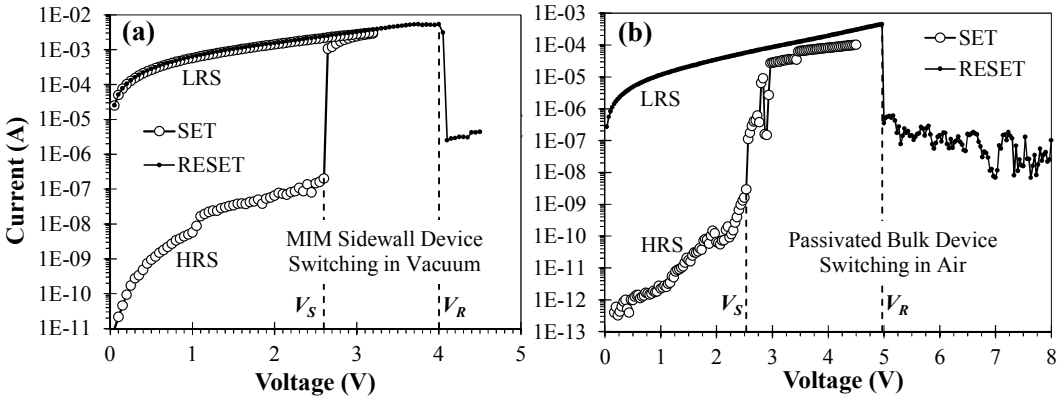

Figure 6. Switching *I-V* response for: (a) MIM sidewall device with TiW electrodes, 60 nm PECVD SiO_2, V_S = 2.6 V, V_R = 4.0 V, switching in vacuum; and (b) MIS bulk device with 51 nm e-beam SiO_2, Pd/Si electrodes, SU8 passivation, V_S = 2.53 V, V_R = 4.97 V, switching in 1 atm air.

In general, a wide range of resistance states can be programed during the RESET process, where device resistance increases as applied voltage increases, which is referred to as the "stop voltage effect." Figure 7 describes the results of varying RESET stop voltage from 5 V to 12 V in 1 V increments in order to investigate the relationship between SET voltage V_S and programed HRS resistance R_{HRS}. A forward voltage sweep up to the stop voltage was used to RESET the device to the HRS, and a forward/reverse voltage sweep to 3.8 V was used to SET the device to the LRS. A total of 80 programing cycles were done on a single MIM device, with 10 cycles done at each stop voltage value. As expected, there was no dependence of LRS Resistance R_{LRS} on stop voltage, where R_{LRS} was determined from the measured I at 1 V. Following the convention used in Ref. [55], $R_{HRS} \equiv V_S / I_S$, where I_S is the current

measured immediately prior to V_S in the *I-V* response (see Figure 6). Both the V_S and the HRS Resistance data show increasing trends with stop voltage in Figure 7a, indicating that these variables are correlated. The scatter plot in Figure 7b confirms that V_S is strongly correlated with R_{HRS}. As discussed further below, this correlation is similar to results found for HfO_2 materials operating in unipolar mode, and is consistent with a cell-based percolation model of the CF [55].

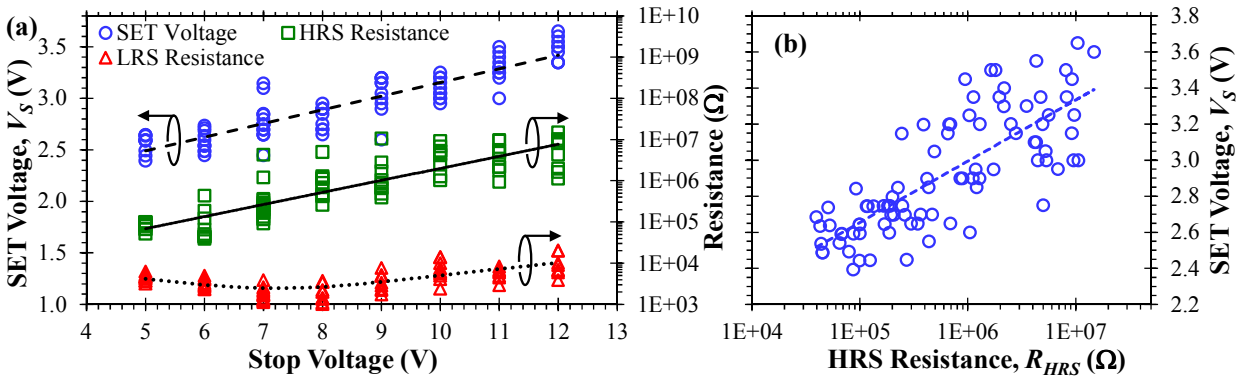

Figure 7. Effects of varying RESET Stop Voltage showing: (a) SET voltage V_S (circles), HRS Resistance (squares) and LRS Resistance (triangles) versus Stop Voltage; and (b) V_S versus HRS Resistance, R_{HRS}. In (a), dashed line is linear fit to V_S data, solid line is exponential fit to HRS Resistance data, and dotted line is polynomial fit to LRS Resistance data. In (b), dashed line is logarithmic fit to V_S data.

III.B.2 Ambient Effects on Resistive switching

Ambient gas effects on electroforming and RS have been previously reported for $TaN/SiO_2/N^+Si$ MIS-edge devices with 60 nm SiO_2 deposited by reactive sputtering [24]. Electroforming in 1 atm N_2 produces devices with operating characteristics similar to devices electroformed in vacuum, although V_{EF} was found to be significantly larger in N_2 (~ 20 V) versus vacuum (~ 8 V). The higher forming voltage in N_2 could be the result of the larger convective heat dissipation by the 1 atm ambient as compared to that of vacuum, which could indicate that electroforming generates high local temperatures near the filament as it is formed, consistent with views that localized heating is necessary for successful electroforming [7, 16]. A study of RS capability as a function of pressure in 20% O_2/N_2 ambient characterized an O_2-induced failure mode where switching is disabled for pressures above 10 Torr (2 Torr O_2 partial pressure). Interestingly, full recovery of RS occurred after the device was cycled at ~ 1 mTorr [24], as explored in more detail below.

Table I lists experimental results investigating the effects of air and pure O_2/N_2 on switching capability of TiW MIM devices (Figure 1b). Averaged *I-V* data are shown in Figure 8 and demonstrate the effects of operating in oxygen-containing ambients. A set of 28 devices were first electroformed and cycled 10 times in vacuum at ~ 0.1 mTorr. Each cycle used a 3.5 V forward/reverse DC voltage sweep to SET the device to the LRS, followed by an 8 V sweep to RESET to the HRS. Half of the devices were left programed to a LRS and half to a HRS. Two sets of 14 devices, each having 7 devices in the LRS and 7 in the HRS, were then given an 8 V RESET sweep and cycled 5 times at 1 atm pressure with one set being operated in air and the other in a high-purity 20% O_2/N_2 mixture. Regardless of ambient, all devices failed to switch after the first 8V sweep. As shown in Figure 8a, LRS devices exhibit a peak in current near 2.5 V followed by a substantial drop in current at ~ 3 V, which are consistent with a typical RESET *I-V* response for devices with low series resistance. As voltage increases to > ~ 4 V, the LRS devices operated in air begin to depart substantially from those operated in O_2/N_2, where the devices operated in air consistently showed a significant reduction in current at 4.4 ± 0.6 V, as compared to the LRS devices operated in O_2/N_2 that had a much more gradual current reduction in the voltage range from 4 – 7 V. The devices previously programed to the HRS in some cases made attempts to switch to the LRS at ~ 3 – 4 V when operated at 1 atm, but none of the devices were successfully programed to the LRS. After the first 8 V sweep in 1 atm ambient, the 28 devices were cycled 5 times and showed no ability to switch state. These results indicate that both the SET transition at ~ 2.5 V and the RESET transition are disabled by O_2, consistent with the hypothesis that the defects responsible for RS are hydrogen-passivated and inert to reactions with O_2 and H_2O in the air [19, 24]. Filaments are thus capable of robust read endurance for several hours when biased to 1 V in air at temperatures up to 150 °C [23], but when the bias increases to above ~ 2.5 V, a switching event occurs and H-passivation is temporarily lost so that defects in the CF can react with O_2 and H_2O.

After attempts to operate in 1 atm ambient, the devices were placed back into vacuum to observe their recovery dynamics by applying a first sweep to 8 V followed by 5 switching cycles. All devices exposed to O_2/N_2 recovered vacuum switching capability immediately after the first 8 V sweep, where a marked increase in current was measured at 4.6 ± 0.8 V as shown in Figure 8b. In stark contrast, RS was not recovered in any of the devices exposed to air, even after the 8 V sweep and the 5 programing cycles. The average of all six 8 V sweeps per device for the 14 devices exposed to air is shown by the dotted line in Figure 8b, which is featureless without any of the current increases observed in devices exposed to O_2/N_2. The 14 devices exposed to air were then subjected to an 8 V

forward/reverse sweep in an attempt to recover vacuum switching capability. If this sweep was not successful, a forward/reverse sweep to 8.5 V was done, and so on in 1/2 V increments until the device recovered. The averaged data for these forward/reverse vacuum recovery sweeps are shown by the solid line in Figure 8b. The average voltage needed to recover the 14 air-exposed devices was 9.5 ± 0.8 V (Table I). Both sets of devices were then cycled again in vacuum for 5 cycles in order to verify recovery of switching capability, where Figure 8c demonstrates that both sets of devices fully recovered and followed the characteristic RS *I-V* response.

These results for near-stoichiometric SiO_2 layers are the exact opposite of results found for highly sub-stoichiometric SiO_x layers with $x < 0.75$, where device switching is severely degraded when operated in vacuum, but when operated in oxygen-containing ambients the *I-V* characteristics show the usual unipolar response with $V_S > V_R$ [56]. The RS model described by Wang *et al*. provides a reasonable explanation for switching in sub-stoichiometric SiO_x layers, where a percolation model involving un-passivated Si dangling bonds is proposed to account for high current in the LRS and passivation of Si dangling bonds by oxygen is thought to RESET devices to the HRS [56]. The contrasting results shown in Figure 8 and the unusual unipolar response with $V_S < V_R$ (Figure 6) clearly indicate that RS mechanisms are different for the near-stoichiometric SiO_2 layers used here as compared with the sub-stoichiometric SiO_x layers characterized by Wang *et al*.

It has been determined using density functional theory (DFT) calculations that O_2 molecules react with Si-Si oxygen vacancies to form peroxy defects ($SiOO^+Si$) at room temperature without any activation energy barrier, where the exothermic reaction with the positive-charged vacancy releases 4.5 eV [45]. This may indicate that switching is disabled in O_2/N_2-exposed devices by peroxy-like defects where O_2 attacks the CF as soon as a bias > 2.5 V is applied so that a switching event creates an un-passivated Si atom. In this case applying a bias > 4.5 V in vacuum may provide enough energy to remove O_2 from the peroxy-like defect and re-establish switching capability. The recovery of vacuum switching capability occurs at ~ 4.6 V in devices exposed to O_2/N_2 (Figure 8b), consistent with removal of O_2 from a peroxy-like defect. This same mechanism could be responsible for the large drop in current at ~ 4.4 V when LRS devices fail during the first 8V sweep in air (Figure 8a), where the removal of the peroxy-like defect could then allow H_2O to attack the defect. Clearly, exposure to O_2 and H_2O in air affects the CF differently than exposure to O_2 alone, and a larger bias of ~ 9.5 V is required to recover devices cycled in air, as demonstrated in Figure 8b. Apparently, attack of the CF by H_2O forms defects that are considerably more stable than the peroxy-like defects formed by reaction with O_2. These results clearly demonstrate that both O_2 and H_2O are

in the immediate vicinity of the CF whenever (unpassivated) sidewall devices are exposed to air, which is not unexpected since the CF is located within several nm of the sidewall surface (Figure 4). Hydrogen-passivated Si is remarkably inert to attack by O_2 and H_2O [57, 58], so that a reasonable explanation for the experimental results is that the CF is comprised of defects that are H-passivated in both the LRS and HRS, except when a switching event occurs and H passivation is temporarily lost.

Table I. Summary of experiment exposing MIM devices to 1 atm of O_2/N_2 or air.

Ambient (1 atm)	# of Devices	1 atm Failure Voltage[1]	Vacuum Recovery Voltage[2]
20 % O_2/N_2	14	4 – 7 V	4.6 ± 0.8 V
Air	14	4.4 ± 0.6 V	9.5 ± 0.8 V

[1] for the 7 devices in each ambient programed to the LRS

[2] after operating 14 devices in 1 atm ambient

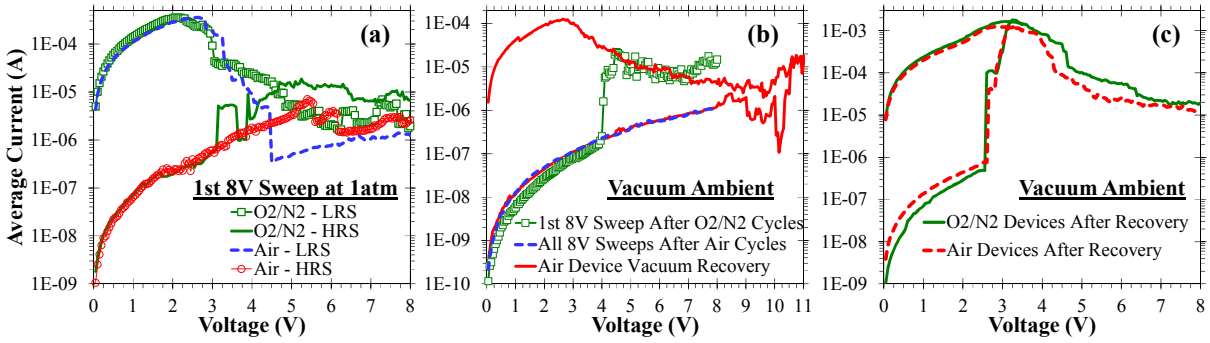

Figure 8. (a) First 8V sweeps in 1 atm ambient (after vacuum electroforming and cycling), averaged for 7 LRS MIM devices in 20% O_2/N_2, 7 HRS devices in 20% O_2/N_2, 7 LRS devices in air, and 7 HRS devices in air. (b) Averaged *I-V* response in vacuum after operating attempts in 1 atm ambient. The average of 14 first 8 V sweeps under vacuum for devices previously cycled in O_2/N_2 indicate recovery of RS at 4.6 ± 0.8 V (square symbols). Eighty-four 8 V vacuum sweeps were averaged for the devices cycled in air without recovery (dashed line). Devices cycled in air recovered after forward/reverse sweeps to an average value of 9.5 ± 0.8 V with one device requiring 11 V (solid line). (c) Average of 3 vacuum RS cycles from each of the 14 devices exposed to 1 atm O_2/N_2 (42 curves, solid line) and air (42 curves, dashed line) after vacuum recovery, indicating a characteristic

unipolar response.

III.C. Low-Frequency Noise Measurements

The noise signature of electronic devices can provide key information regarding the defects involved in charge transport. As shown in Figure 9, low-frequency (f < 10 kHz) noise measurements were performed on a set of 10 TaN MIS devices under DC bias of 0.1, 0.4, 0.8, 1.2 and 2.5 V. Five devices were programed to the LRS and five to the HRS prior to the experiment. The power spectral density was estimated using Welch's modified periodogram method [59]. Data analysis methods similar to those described in Ref. [60] were implemented here using an Agilent B1500A semiconductor device analyzer and digital oscilloscope for data storage. No significant trends were observed with DC bias. After normalizing the power spectral density data to its noise base, the data in Figure 9 reveal a $1/f$ noise signature in the LRS and a $1/f^2$ response in the HRS. The $1/f$ response indicates that a large number of defects are involved in LRS charge transport, whereas the $1/f^2$ signature indicates transport through a very small number of electrically-active defects in the HRS [61, 62]. Investigations of random telegraph noise (RTN) and temporary RTN in MOS devices have associated similar noise signatures with transitions between switching charge-state energy levels and related structural relaxations of electron-trapping defects [63-65]. As a result, the noise measurements in Figure 9 support a model where the defects involved in charge transport are electron-trapping defects.

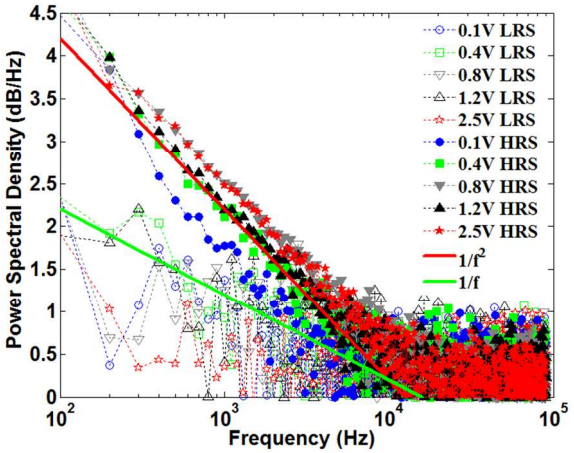

Figure 9. Normalized noise power spectral density

measurements for 5 TaN MIS devices set to the LRS and 5 devices set to the HRS. Green line is $1/f$ trend and red line is $1/f^2$ trend.

IV. Device Operating Models

The motivation for this study was to determine whether interactions between known SiO_2 defects could provide plausible electroforming and RS models. Based on the experimental observations described above, it is clear that electroformation products must have at least three key properties: 1) they must be stable under moderate bias ($V < 2$ V) when exposed to ambient air; 2) they must be capable of reversible RS; and 3) electroformation products must have energetics that match the unipolar *I-V* response. The sub-sections below first present a conceptual physical model of the conductive filament, followed by a brief review and discussion of SiO_2 defects to help identify candidate electroforming products having the above key properties. The electronic and electrochemical characteristics of candidate defects are then used to formulate electroforming and RS models that are further demonstrated to be consistent with the prominent features in the *I-V* response. Electron energy band diagrams are constructed for the LRS and HRS in order to further quantify potential RS mechanisms. Charge transport modeling provides support for the proposed RS models. Finally, many of the unusual operating characteristics observed in SiO_2 RM devices are explained by the electroforming and RS models.

IV.A Physical Model of Conductive Filament

The fact that both electroforming (Figures 2 and 3) and oxide BD [28, 29] are associated with a threshold current of ~ 1 μA leads to the question of whether oxide breakdown mechanisms may play a direct role in SiO_2 electroforming. Oxide BD is generally recognized as being the result of accumulated point defects created by current flow through the oxide, leading to electron traps at interfaces, traps in the SiO_2 bulk and anomalous positive charge [66]. Multiple mechanisms are thought to occur during oxide degradation and BD, including: hot electron and hole injection having threshold energies ranging from 2 to 9 eV; oxide band-gap impact ionization that can occur above ~ 9 eV; a process attributed to either anode hole injection or hydrogen release at ~ 5 eV and below; and trap creation involving atomic hydrogen at ~ 2 eV [66]. Despite over half a century of research into the electrical properties of

SiO_x materials, the detailed microscopic mechanisms responsible for oxide BD and MOS device degradation continue to be vigorously debated [63, 66, 67]. According to most models, BD occurs when a critical density of point defects forms a percolation pathway of electron traps within the dielectric [66].

Most explanations of electroforming in SiO_x materials describe the Si-rich CF as being formed primarily by oxygen reduction mechanisms [5, 7, 11, 16, 21, 25, 56, 68]. In oxide layers with thickness greater than 10 nm, such as those used here, electrons injected by Fowler-Nordheim (F-N) tunneling into the oxide conduction band are believed to reach steady-state conduction with average energy of ~ 6 eV when the electric field is in the range of 8 – 12 MV/cm [66]. High-energy electron impacts can presumably break Si-O bonds to release O^{2-} ions and form Si-Si oxygen vacancy defects, leading to a percolation pathway that contributes to oxide breakdown when a critical defect density is reached [66]. The electric fields for the un-annealed and N_2-annealed devices in Figure 2 range from 2.5 – 9.7 MV/cm, so that it is reasonable to expect that similar percolation pathways are created by the electroforming process during the forward voltage sweep. In contrast, all devices in Figure 2 that were treated with H_2- or D_2-containing anneal electroform within a lower range of electric fields from 1.0 – 2.0 MV/cm, indicating that the introduction of H or D into the SiO_2 layer reduces the energy needed for electroforming. As discussed briefly above, during reducing anneal as-deposited Si-Si defects are terminated by H to form Si-HH-Si, or $(SiH)_2$ [42, 43]. The H-bridge defect, Si-H-Si, can potentially provide a low-energy pathway for oxygen reduction [25]. The Si-H-Si defect is readily formed by charging the $(SiH)_2$ defect positive, which brings the two H atoms closer together and increases the probability for H_2 dissociation and proton release [43, 69]. Once formed, Si-H-Si can potentially promote the oxygen reduction reaction by forming its positive-charged interconversion product [25], where one of the Si atoms back-bonds to a network oxygen atom to form $SiH+SiO(3)^+$ [43]. The 3-fold-coordinated O atom in this configuration is likely able to diffuse away [43], leaving behind the original Si-H-Si and a newly-formed Si-Si defect. This low-energy oxygen reduction mechanism may be one reason that H- and D-containing anneals significantly reduce V_{EF}. Another reason why reducing anneal lowers V_{EF} could be that Si-H-Si is directly involved in RS, as discussed further below.

While such defect-related percolation pathways are typically believed to be responsible for stress-induced leakage current (SILC), soft breakdown (SB) and time-dependent dielectric breakdown (TDDB) in MOS devices [43, 46, 67, 70-74], it is clear that mechanisms other than simply forming a percolation pathway must occur during electroforming to account for the observed RS behavior in SiO_2-based RM devices. Figure 10 illustrates some

mechanisms that may occur during the electroformation process. Figures 10a and 10b show two possible outcomes when an O^{2-} ion is released, either by high-energy electron impacts or with the aid of positive-charged Si-H-Si defects, as described above and as depicted in Figure 10a. As the O^{2-} ion drifts in the applied field towards the positive-charged anode, it can potentially react with a Si-Si defect to form Si-O-Si, the net result being the diffusion of one Si-Si defect to a location adjacent to the Si-H-Si defect – a so-called "clustering" effect [43]. Alternatively, the O^{2-} ion could diffuse or drift to the sidewall surface and be lost to the vacuum, or it could reach an interface where it may react and become neutralized, with the net result in both cases being a localized increase in Si concentration. These outcomes are depicted in Figure 10b, where the top part of the figure shows the result for Si-Si diffusion and the lower part shows the result for increased Si content. Since the CF is located within a few nm of the sidewall surface (Figure 4), a substantial fraction of the O^{2-} generated during electroforming can potentially be released into the vacuum and removed from the percolation pathway as it forms, and this could be the primary reason why successful electroforming requires a vacuum or non-oxidizing ambient. It may be noted that the H atom in Si-H-Si can potentially migrate to a nearby Si-Si defect and form an interconversion product with another network O atom, so that each Si-H-Si could possibly create multiple O^{2-} ion/Si-Si pairs. As O^{2-} ions are released and drift away, Si-Si defects would tend to cluster near the Si-H-Si defect, potentially forming a localized reduction in oxide density, or pore. This mechanism could lead to high pore concentration along the percolation pathway. As a result, Si-H-Si could be an efficient catalyst for Si-rich defect clustering where porous regions along the pathway may further trap mobile species and support the electrochemical reactions that lead directly to RS. Given that positive-charged defects, D(+), and negative-charged defects, D(–), will drift in opposite directions, and since they will have a coulomb attraction, there will be a high probability that opposite-charged defects will interact during the forming process, as depicted schematically in Figures 10a and 10b. Such interactions may transform the percolation pathway into a CF capable of supporting RS. The implications of these processes and specific charged defects that may be involved are addressed in the following sections, leading to plausible models for electroforming and RS.

Figures 10c – 10e show a physical model of the CF. The overall structure of the CF is similar to geometrical cell-based percolation models that are analogous to models of oxide breakdown [2, 9, 55, 75] and other physical models [5, 10, 21, 28, 56, 76], except that the CF is located within ~ 4 nm of the sidewall surface (Figure 10c) in accordance with the Figure 4 results. The CF is allowed to become wider in the plane of the sidewall surface [20], consistent with electroforming being fundamentally a near-surface phenomenon. In regions where a large number of defects

cluster together, Si nanocrystals can form, as observed in several TEM studies [6, 7, 16]. In line with previous reports [2, 19, 22, 26, 76], a narrowed region along the CF is most likely where RS takes place. The minimum LRS resistance in Figure 7a is R_{LRS} ~ 1000 Ω, which is a factor of 12.9 smaller than the reciprocal of the quantum conductance $G_0^{-1} = h/2q^2$ = 12,900 Ω, where h is the Plank constant and q is the elementary charge [76]. This suggests that, for the device measured in Figure 7, the switching region contains about 13 parallel pathways that support current in the LRS, whereas R_{HRS} ranges from about $10G_0^{-1}$ to $1000G_0^{-1}$ so that a physical gap has likely formed in the CF in the HRS [9, 77]. Regardless of whether RS is due to electrochemical, valence-change, or thermochemical mechanisms, defects are thought to play the key role in switching behavior [2]. Unlike most other operating models, the model adopted herein accounts for the possibility that the defects responsible for RS may remain localized within the switching region. In this case, each defect in the switching region can be in a conductive "ON" state or a non-conductive "OFF" state, leading to a model where a device programed to the LRS has a large concentration of ON-state defects within the switching region (Figure 10d). Conversely, when the device is programed to the HRS, a significant number of defects are converted to the OFF state, thus forming a conductance "gap" in the CF with length l_{GAP} (Figure 10e). By measuring devices with a range of SiO_2 thicknesses and using electrical breakdown measurements, the maximum length of the switching region (l_{SW}) has previously been estimated to be in the range from l_{SW} ~ 6 – 10 nm [20].

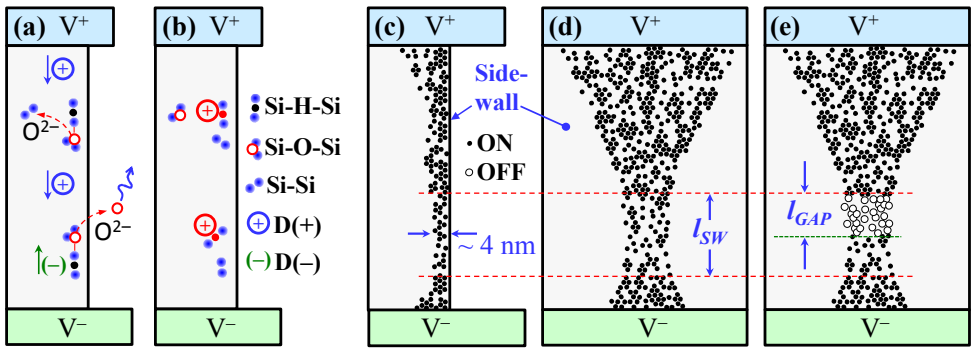

Figure 10. Schematic representation of defects near SiO_2 sidewall illustrating: (a) oxygen reduction and ion drift mechanisms that may occur during electroforming; (b) the results of oxygen reduction and ion drift mechanisms possibly leading to the defects responsible for RS; (c) cross-section view of sidewall region after forming CF with ~ 4 nm lateral depth into SiO_2 sidewall; (d) front-on view of sidewall in LRS where all defects in switching region

l_{SW} are in their ON state; and (e) front-on view of sidewall in HRS where defects within l_{GAP} are in their OFF state. Dashed lines mark the switching region with length l_{SW}. Illustrated gap length is $l_{GAP} \sim l_{SW}/2$.

IV.B. SiO_2 Defect Review

Figure 11 shows schematic representations of several extensively-studied, common SiO_2 defects. Many reports are available describing their detailed electrical and structural properties [42, 43, 45, 48, 49, 66, 70, 78-81]. Table II lists the charge states, switching charge-state energy levels, thermodynamic energy level (E_{TH}) and effective bandgap (ΔE_G) for five of the defects in Figure 11 based on DFT calculations in α quartz [43]. Calculating these energy levels relative to a given reference such as the Si bandgap is difficult [49], and there are few reports providing quantitative values [43, 70, 80]. The energy levels of defects in amorphous SiO_2 depend on the local atomic arrangement so that a range of values will be associated with each switching charge-state and thermodynamic energy level [80, 81]. Nevertheless, the values listed in Table II provide a meaningful relative comparison of the various defects. The ΔE_G energy is the difference between the un-occupied charge-state energy level (E_C), typically associated with an effective conduction band-edge, and the occupied charge-state energy level (E_V) associated with an effective valance band-edge. Those defects having small ΔE_G and charge-state energies near the Fermi levels of the electrodes are typically considered to be conductive since electrons are loosely bound when trapped by the defect and the relaxation energy of the defect is small [66, 70].

The Si-Si defect is the dimer oxygen vacancy where a weak bond is established between the two Si atoms [43, 80, 81]. This defect has large ΔE_G and a E_{TH} far from most common electrode Fermi levels, and is thus considered to be non-conductive. The Si-Si defect has an interconversion product, $Si^*SiO(3)^+$, where one of the Si atoms back-bonds to a network O atom in a "puckered" configuration with the network O atom becoming 3-fold coordinated and positive-charged, leaving the remaining Si atom with a dangling bond (Si*) [81]. The $Si^*SiO(3)^+$ defect has small $\Delta E_G \sim 1.7$ eV and E_{TH} near the Si midgap (Table II) so that it is conductive.

In general, RS in devices having a CF can involve electrochemical, valence-change, and thermochemical mechanisms [2], making it important to understand that RS in different materials may involve different mechanisms. Although thermal dissolution models involving oxygen vacancy creation/annihilation or defect diffusion into and out-of the CF provide reasonable explanations for RS in unipolar devices using HfO_2, NiO and TiO_2 materials [2, 9, 55, 75, 77, 82, 83], there is no *a priori* reason to assume that the same mechanisms occur in SiO_2 materials. While

drift of O^{2-} ions and diffusion of oxygen vacancies is often used to describe RS in RM devices based on metal oxides or embedded nanoparticles [84-86], the Si-Si and Si*SiO(3)$^{+}$ oxygen vacancy defects are not likely involved in SiO_2 RS for the following reasons. A model involving Si-Si oxygen vacancy defects cannot account for the observed ambient effects. As described above, the CF is formed within ~ 4 nm of the sidewall surface (in sidewall devices), and is exposed to O_2 and H_2O vapor whenever the (unpassivated) device is exposed to air. The reaction of O_2 with Si-Si proceeds without an activation energy barrier to form $SiOO^{+}Si$ [45]. Also, H_2O vapor in the air would react with Si-Si defects under small applied bias ~ 1.3 – 1.8 eV to form SiH and SiOH [45]. Since exposure to O_2 is found in Figure 8 to disable switching, and since SiH and SiOH are considered to be electrically inert [43, 79], the reactions of oxygen vacancies with O_2 and H_2O would be expected to alter programed data if oxygen vacancy defects were involved in RS. However, this is inconsistent with results showing that programed states in un-passivated devices remain nonvolatile after many months of air exposure [21]. Furthermore, a switching model based on Si-Si creation/annihilation driven by O^{2-} ion drift cannot account for unipolar operation because ions will drift in the same direction during both SET and RESET programing events, making it very difficult to explain where the O^{2-} ions go and how they return to the switching region. In another potential scenario involving oxygen vacancies, the Si-Si and Si*SiO(3)$^{+}$ defects could potentially be driven between the two structural configurations Si-Si + Si-O-Si ↔ Si*Si-O^{+}=Si_2 to perform switching operations since Si-Si is nonconductive and Si*SiO(3)$^{+}$ is conductive, similar to some oxide degradation models [63]. However, it must be noted that Si*SiO(3)$^{+}$ stability is highly-dependent on local atomic arrangement and some forms collapse immediately to the Si-Si defect upon capture of an electron [43, 80, 81], making it doubtful that this defect pair could sustain long-term RS. As a result, the instability of the Si-Si and Si*SiO(3)$^{+}$ defects with regards to reactions with O_2 and H_2O, and the incompatibility with unipolar operation make it unlikely that these defects are involved in RS.

As described above, the $(SiH)_2$ defect is formed during anneal in H_2-containing ambients by the reaction Si-Si + H_2 → $(SiH)_2$ [42]. This defect has E_{TH} and ΔE_G energies similar to those of the Si-Si defect, and is thus non-conductive. However, it is relatively stable due to the two H-passivated SiH groups. As discussed further below, the threshold energy for H desorption from the SiH group is ~ 2.5 eV [39, 46, 87-89], essentially the same as the SET transition of V_S ~ 2.5 V in the *I-V* response (Figures 6 and 8c). This makes the $(SiH)_2$ defect a good candidate for an electroformation precursor since desorption of a H atom forms the conductive H-bridge [69].

The H-bridge defect, Si-H-Si, has small ΔE_G ~ 1.71 eV and is found using DFT calculations to form a conductive

defect that has been proposed as being responsible for SILC, BD and TDDB in MOS devices [43, 46, 67, 70, 71], thereby warranting further investigation both as an electroformation precursor and possibly the defect responsible for high conductance in the LRS. The Si-H-Si defect interconverts to the negative-charged defect $SiH+SiSi(5)^-$ when one of the Si atoms back-bonds to a network Si atom (which becomes 5-fold coordinated), and to the positive-charged defect $SiH+SiO(3)^+$ when a Si atom back-bonds to a network O atom [43]. As described above, the positive-charged interconversion product can potentially lead to the oxygen reduction reaction and increased porosity during electroforming.

The $(SiOH)_2$ defect is absorbed water where the Si atoms in the two SiOH (silanol) groups are 4-fold coordinated. The silanol groups are not to be confused with mobile OH^- ions that are loosely bound to Si atoms in the network (which become 5-fold coordinated) and can migrate through the amorphous network by hopping between Si atoms with an activation energy of only ~ 0.6 eV [34]. Instead, the silanol groups in $(SiOH)_2$ are structurally stable up to ~ 700 K [31], and can form in amorphous SiO_2 by the dissolution of H_2O in reactions that range from endothermic to exothermic, depending on the amount of strain present at the network reaction site [34]. At SiO_2 surfaces exposed to air, such as SiO_2 sidewalls in unpassivated devices, SiOH density approaches 3.8 molecules/nm^2 [35], thus essentially providing an infinite supply of OH to the percolation pathway that forms within nanometers of the sidewall surface (Figure 4).

The Si_2=O-H_3O^+ defect can form by the reaction of two H_2O molecules or by proton uptake by H_2O. In the 1990s, E. H. Poindexter developed a hydrogen physical chemistry model to investigate potential reactions of H_2O in SiO_2, leading to the postulation that $2H_2O \rightarrow H_3O^+ + OH^-$ [31]. This reaction was verified in 2002 using first-principles DFT calculations finding that $2H_2O$ in "bigger voids" react to form a mobile OH^- ion and a *localized* H_3O^+ ion that may contribute to positive fixed-charge in as-deposited SiO_2 materials, where the H_3O^+ ion attaches to an O atom in the Si-O-Si network to form Si_2=O-H_3O^+ [45]. The presence of H_3O^+ has long been established in weak ionic solutions [90] such as HF and H_2O, where the reversible reaction $HF + H_2O \leftrightarrow F^- + H_3O^+$ is known to occur [91]. Since SiO_2 is also a weak ionic medium, it is reasonable to expect that H^+ uptake by H_2O will occur in SiO_2 to form H_3O^+. In fact, DFT calculations have established that H^+ uptake by interstitial H_2O can form H_3O^+ near Si/SiO_2 interfaces when SiH and a hole are present, which proceeds with only a ~ 0.8 eV reaction barrier and ~ 0 eV forward energy [31, 48, 92]. In addition, experimental data link trace amounts of H_2O in thermal oxides to bias-temperature instability (BTI) in MOS devices as a result of this mechanism [93]. Using a new dissociative water potential, recent

molecular dynamics simulations of H_2O adsorption onto SiO_2 surfaces reveal a new mechanism for dissociative chemisorption involving the formation of H_3O^+ as a reaction intermediate, leading to SiOH formation at non-bridging oxygen (Si-O^-) and Si* defects in the near-surface region [35]. In this case the H_3O^+ ion participates by providing an efficient pathway for H^+ transfer to adjacent H_2O molecules until the H^+ finds a Si-O^- to form SiOH [35]. These findings make it reasonable to expect that similar proton exchange reactions will occur in bulk SiO_2 materials, especially near SiO_2 surfaces previously exposed to water vapor. Therefore, as a stable [31], localized, positive fixed charge [45], the H_3O^+ ion is a very good candidate for an electroformation precursor or product since it can potentially release a H^+ to leave a H_2O molecule that is then available for H^+ uptake in a reversible reaction depending on the local charge environment.

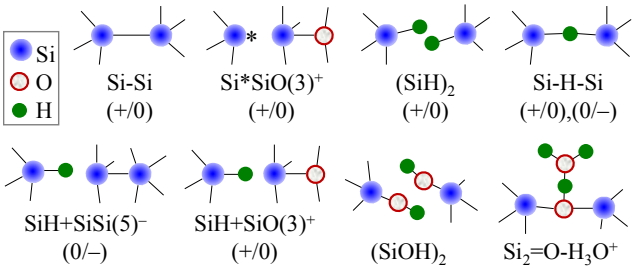

Figure 11. Some of the known defects in SiO_2. Switching charge states are labeled: (+) positive, (0) neutral and (–) negative.

Table II. Defect positive (+), neutral (0) and negative (–) switching charge-states, unoccupied switching charge-state energy levels (E_C), thermodynamic energy levels (E_{TH}), occupied switching charge-state energy levels (E_V) and effective bandgap energies (ΔE_G) referenced to the Si midgap energy in units of eV [43].

Defect	**Charge-States**	**E_C**	**E_{TH}**	**E_V**	**ΔE_G**
Si-Si	+/0	-1.38	-3.03	-3.70	2.32
Si*SiO(3)$^+$	+/0	0.68	-0.06	-1.02	1.70

$(SiH)_2$	+/0	-1.07	-2.74	-3.67	2.60
Si-H-Si	0/–	1.58	0.74	-0.13	1.71
Si-H + $SiSi(5)^-$	0/–	1.27	0.30	-1.85	3.12

IV.C. Electroforming Model

As described briefly above in the discussion surrounding Figures 2, 3 and 10, for the electroforming electric fields of 1 – 10 MV/cm, hot electrons and holes with energy > ~ 9 eV may create Si-Si defects and O^{2-} ions by oxide BD mechanisms such as band-gap impact ionization [66]. In devices with a sidewall etched into the SiO_2 layer, O^{2-} ions created near the sidewall surface may enter the vacuum or may drift towards the anode until they encounter other defects or until they reach the anode interface where they react and become neutralized (Figures 10a and 10b). In bulk devices, drift and diffusion of O^{2-} ions may be enhanced by pin-hole defects or other low-density regions in the porous, e-beam-deposited SiO_2 layer. In both device types, these mechanisms allow O^{2-} ions to be removed from the immediate vicinity of the percolation pathway as it forms, thus leaving behind reactive Si-Si defects. Protons (H^+) are expected to form by high-energy electron impacts at the anode/oxide interface, where the so-called hydrogen release mechanism requires ~ 5 eV for a H^+ to be created at the anode and to drift into the bulk region of the oxide layer [46, 66]. In addition, the large amount of SiOH in near-surface regions of the sidewall (in devices with a sidewall) or near the cathode/oxide interface (in bulk devices) may be a good source of loosely-bound OH^- ions. When an OH^- ion encounters a hole in the oxide, the O atom reacts with the oxide network to form a SiOOSi structure and a H^+ is released [34]. It is thus well-documented that large H^+ concentrations are created in oxides previously exposed to H_2O vapor and placed under a high electric field, and it is therefore reasonable to expect similarly high H^+ concentrations during electroforming of SiO_2-based RM devices having an exposed sidewall and in bulk devices using porous oxide materials deposited at low temperatures.

It may be noted that several research groups have reported potential roles for water-related defects in RM devices. Shang *et al.* suggested that RS in tungsten oxide RM could be supported by proton transfer as the result of surface H_2O decomposition [94]. Recently, the possibility that protons could perform the same function as O^{2-} ions during device RESET in TiO_{2-x} devices was proposed by Park *et al*. [95]. Using Raman spectroscopy on RM devices

incorporating SiO_2 and other switching materials, Shoute *et al.* detected a polaron signature only when devices were capable of RS, and found that switching could not be initiated unless the device contained a trace amount of H_2O [96].

Based on the above discussion related to the defects shown in Figure 11, the most intuitively obvious candidates for SiO_2 electroformation precursors are Si-H-Si and Si_2=O-H_3O^+. As the H^+ drifts through the oxide towards the cathode, it may encounter Si-Si to form Si-H-Si [43, 46, 50, 66]. As described above, conductive Si-H-Si defects also form by H desorption from $(SiH)_2$. As soon as the concentration of conductive defects reaches a critical threshold, a percolation pathway forms and current reaches ~ 1 μA at V_{EF} (Figures 2a and 3). However, a percolation pathway by itself cannot support RS, so that additional electrochemical reactions or other transformations must occur. As mentioned above, oxide materials deposited at low temperature are typically porous and susceptible to H_2O absorption [31, 32, 34-36]. As a result of high-energy electron impacts at defect sites along the percolation pathway, locally high temperatures may result from Joule heating, which will enhance H_2O diffusion and increase the probability that two H_2O molecules will diffuse to a pore and react to form a localized H_3O^+ ion and a mobile OH^- ion. Alternatively, a H_2O molecule may simply uptake a H^+ to form H_3O^+. The H_3O^+ ion in a pore attaches to a network O atom to form localized Si_2=O-H_3O^+, which will present a coulomb attraction for any negative-charged species that may drift or diffuse near the ion. The Si-H-Si defect in its most stable form is charged negative [43], making it reasonable to model the electroforming reaction as

$$2e^- + \text{Si-H-Si} + Si_2\text{=O-}H_3O^+ \rightarrow \text{Si-}H^-\text{-Si} + H^+ + \text{Si-O-Si} + H_2O \rightarrow (SiH)_2 + (SiOH)_2. \quad (1)$$

Two electrons initiate the reaction in (1), one that charges the neutral Si-H-Si defect negative and one injected into H_3O^+ to release a H^+. The exothermic reaction of Si-H^--Si and H^+ forms $(SiH)_2$ and releases ~ 3 eV of energy [43], which is about twice the energy barrier required to form two silanol groups by the water absorption reaction Si-O-Si + $H_2O \rightarrow (SiOH)_2$ [34, 45, 97]. Once the $(SiH)_2$ and $(SiOH)_2$ defects form in close proximity to each other, the conditions for RS are established at that location.

It may be noted that the product complex in (1) can be viewed as two H_2O molecules reacted with two oxygen vacancies, so that an overall reaction equivalent to (1) is

$$2\text{Si-Si} + 2H_2O \rightarrow (SiH)_2 + (SiOH)_2. \quad (2)$$

From another perspective, the product complex in (1) can be viewed as a H_2 molecule reacted with an oxygen vacancy and a H_2O molecule reacted with the oxide network, so that another overall reaction equivalent to (1) is given by

$$\text{Si-Si} + H_2 + \text{Si-O-Si} + H_2O \rightarrow (SiH)_2 + (SiOH)_2. \quad (3)$$

The $(SiOH)_2$ defect is electrically inert [43, 79] and structurally stable [31]. The $(SiH)_2$ defect is also an inert, non-conductive defect, as described above. In addition, the Si atoms in $(SiH)_2$ are H-passivated and the Si atoms in $(SiOH)_2$ are OH-passivated, so that both defects are expected to be stable against reaction with O_2 and H_2O vapor in air. As a result, the reaction products in (1) form a complex exhibiting one of the key properties listed above for viable electroformation products. The next sections describe how the energetics and electrochemical reactions of the defects in (1) are consistent with the RS transitions in the *I-V* response, thus satisfying the remaining two criteria for viable electroformation products.

IV.D. Resistive Switching Model

Several studies have used TEM to document the presence of Si nanocrystals within the CF [6, 7, 16]. In some studies, RS is proposed to occur by a change in nanocrystal size, where increased size brings neighboring crystals closer together to decrease tunneling distance and thus increase conductivity [6]. Another view of RS describes how the nanocrystals may transform between amorphous and crystalline phases to account for the HRS and LRS, respectively [7]. Unfortunately, TEM is not capable of detecting isolated defects or the composition of conductive regions that may exist between nanocrystals, thus making it difficult to discern the physical boundaries of the CF. Therefore, it is not yet clear whether either of the above descriptions are valid. A more conventional model is adopted here that relates RS to defect transformations near the nanocrystal surfaces and in the regions between nanocrystals, similar to models described by Mehonic *et al*. for switching in Si-rich oxides [5]. This approach is consistent with findings that charge transport occurs primarily along grain boundaries in NiO and HfO_2 memory materials [3, 8], where oxygen vacancies are thought to be the electron traps most likely involved in RS. This view

is also consistent with models describing RS as occurring at a narrowed "constriction" along the conductive filament [2, 9, 10, 28, 76]. In general, the model presented below is consistent with analytical cell-based percolation models of oxide breakdown where switching statistics are modeled using the Weibull distribution and switching occurs by creation and annihilation of conductive defects within a small switching region along the CF [2, 55, 75]. The model presented below differs from most models by considering that the defects responsible for RS may remain localized within the switching region so that RS occurs when a collection of defects are driven between conductive and non-conductive forms, as depicted in the CF physical model shown in Figures 10c – 10e.

The same electrochemical reactions that form the CF must also be involved in RS. When the reaction in (1) occurs, the conditions for RS are established at that location. The electroforming process may continue until a network of $(SiH)_2/(SiOH)_2$ defect pairs form, thus transforming the percolation pathway into a CF capable of sustaining RS. The reverse reaction of (1) occurs when a H^+ is desorbed from a SiH group in the $(SiH)_2$ defect, which is then available for uptake by the absorbed H_2O molecule. This line of reasoning leads to a plausible RS model given by the reversible electrochemical reaction

$$(SiH)_2 + (SiOH)_2 \leftrightarrow Si\text{-}H\text{-}Si + Si_2{=}O\text{-}H_3O^+ \quad (4)$$

where the forward reaction switches the complex ON and requires a voltage drop across the switching region large enough to induce H^+ desorption from $(SiH)_2$, and the reverse reaction switches the complex OFF and requires injection of $2e^-$ as described by (1).

The conductive (ON) and non-conductive (OFF) configurations of the defect complex, as well as the events that may trigger the defect transitions, are shown pictorially in Figure 12. Starting from the ON configuration (top of Figure 12), electron injection into the H_3O^+ defect releases a H^+ (right-side intermediate state) that reacts electrochemically with Si-H-Si to form $(SiH)_2$ and $(SiOH)_2$, which is the OFF configuration (bottom of Figure 12). When the $(SiH)_2$ in the OFF configuration is charged positive, H^+ desorption occurs (left-side intermediate state) and the H^+ reacts with $(SiOH)_2$ to re-form H_3O^+ and Si-H-Si, which switches the complex back to the ON configuration. Both ON and OFF configurations are stable for voltages $< \sim 2.5$ V and are inert to reactions with O_2 and H_2O in the air since they are H- or OH-passivated and contain no dangling Si bonds, reactive Si-Si bonds or non-bridging O atoms.

When most of the defect complexes within the switching region are in their ON state, the device is in the LRS shown in Figure 10d, whereas the HRS corresponding to Figure 10e occurs when a significant fraction of the complexes are transformed into their OFF state to form a conductance gap within the switching region. While perhaps there are many other defects that could account for RS in SiO_2, the reversible electrochemical reaction given by (4) and shown in Figure 12 provides a straightforward, plausible description of RS in SiO_2 materials.

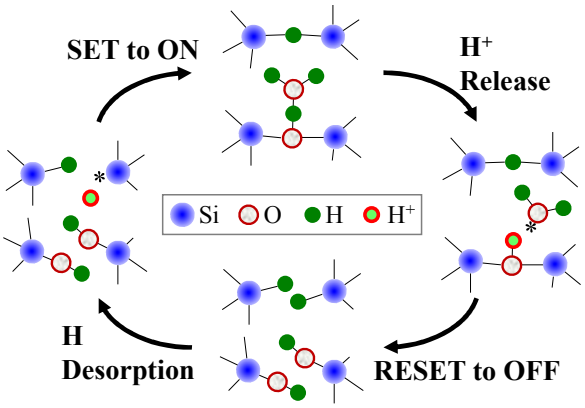

Figure 12. RS model defect transitions. ON state (top) contains Si-H-Si and Si_2=O-H_3O^+. Electron injection into H_3O^+ releases a proton (right-side intermediate state). Electrochemical reaction between the proton (H^+) and Si-H-Si forms $(SiH)_2$ and water absorption forms $(SiOH)_2$ to switch the complex OFF (bottom). Charging $(SiH)_2$ positive leads to H^+ desorption from SiH (left-side intermediate state). Proton uptake by absorbed water forms Si_2=O-H_3O^+ and switches the complex ON (top).

The energetics of the $(SiH)_2$ defect are found to be consistent with the SET transition observed in the *I-V* response. Hydrogen desorption from SiH has long been established to occur at Si/SiO_2 interfaces in MOS devices with a threshold energy in the range of 2.5 – 2.9 eV [39, 46, 87-89], which correlates well with the SET transition at 2.5 – 2.6 V observed in Figures 6 and 8c. As described in Figure 12, the desorbed H^+ may react with absorbed H_2O

to form H_3O^+ in the ON-state complex. In addition, the effective bandgap of $(SiH)_2$ is $\Delta E_G \sim 2.6$ eV (Table II), so that a voltage of 2.6 V must be applied across the switching region before trap-assisted tunneling (TAT) can occur [43, 70]. The TAT current will charge and discharge the $(SiH)_2$ defect to positive and neutral charge states, respectively (Table II). Each time the defect is charged positive, there is a finite probability for proton desorption, which leaves behind the conductive Si-H-Si defect [43, 69]. Furthermore, recent measurements have documented green electroluminescence when similar SiO_x devices are operated in the HRS [6]. The green electroluminescence with peak energy of 2.3 eV was attributed to electron/hole recombination, which would naturally occur during TAT through a defect with bandgap near this energy, such as $(SiH)_2$ with $\Delta E_G \sim 2.6$ eV. Based on these correlations, hydrogen desorption from $(SiH)_2$ is indeed a plausible mechanism to trigger the SET transition at $V_S \sim 2.5$ V (Figures 6 and 8c).

Although the RESET process in many materials is often described as being thermally-driven [2, 5, 9, 15, 16, 55, 77, 82, 83], other mechanisms could also be active in SiO_2 materials. Since the H_3O^+ defect in SiO_2 is characterized as a fixed positive charge, its energy level will be high in the SiO_2 bandgap, near the conduction band-edge [45, 49]. As a result, electron injection into the defect will occur when the voltage across the switching region aligns the conduction band in the CF with the energy level of the H_3O^+ defect. As described in Figure 12 and by (1), electron injection into the H_3O^+ defect is expected to release a H^+ that reacts with $Si\text{-}H^-\text{-}Si$ to form $(SiH)_2$, thus switching the complex to its OFF state and providing an effective RESET mechanism. Similar to a thermally-driven process, the electron injection mechanism also provides a natural explanation for the increasing device resistance with increasing stop voltage (see Figures 5 and 7), where the conductance gap in the switching region (Figure 10e) grows larger as the applied RESET stop voltage increases.

The SET and RESET switching transitions can be described in more detail with the aid of electron energy band diagrams. The band diagrams in Figure 13 were constructed using the thermodynamic and switching charge-state energy levels listed in Table II, as reported by Peter Blochl in 2000 [43]. The unoccupied switching charge-state energy levels of the defects are associated with an effective conduction band-edge, whereas the occupied levels are associated with an effective valence band-edge, thus forming an effective bandgap. To determine the relative band offsets, the standard methodology used for semiconductors was employed where the thermodynamic energy level of each defect was aligned to the electrode Fermi levels at 0 V bias, thus pinning the thermodynamic energy levels of the defects to the electrode Fermi level [43]. The ideal band diagrams in Figure 13 assume electrodes with Fermi

levels at the Si midgap energy and mono-energetic defect energy levels. Defect spacing is assumed to be uniform with one defect cluster every 1/2 nm, which is based on the average electron hopping distance determined by fitting the low-voltage *I-V* response to the hopping conduction expression [26].

In the LRS shown in Figure 13a, the CF is comprised of conductive Si-H-Si and positive-charged H_3O^+. Since Si-H-Si and SiH+SiSi(5) are expected to form with approximately equal concentrations in amorphous SiO_2 [43], both defects are included in the CF, where Si-H-Si has an effective bandgap of 1.71 eV and the bandgap of SiH+SiSi(5) is 3.12 eV, as listed in Table II. Hopping transport through the effective conduction bands of Si-H-Si and SiH+SiSi(5) is presumed to be responsible for the relatively high conductivity associated with the LRS. As electrons hop along the CF from Si-H-Si to SiH+SiSi(5), they encounter an energy barrier of ϕ_{LRS}, which is the relative conduction band offset between the two defects after aligning their E_{TH} levels at 0 V. For the mono-energetic defect energies listed in Table II, ϕ_{LRS} = 0.13 eV is calculated, in reasonable agreement with the electron energy barrier of ~ 0.1 eV measured in devices programed to the LRS [26].

The energy level of H_3O^+ is placed 2.5 eV above the Si-H-Si conduction band to account for the 2.5 V threshold previously identified for the RESET transition [22, 54]. The length of the switching region as drawn in Figure 13a is l_{SW} ~ 5 nm. The voltage across the switching region is given by $V_{SW} = V_A - I_R R_S$, where V_A is the applied voltage, I_R is the RESET current, and R_S is the series resistance. To draw Figure 13, it is assumed that I_R = 2.63 mA, the external series resistance is zero and the internal series resistance of the CF (in filament regions outside the switching region) is 50 Ω so that total series resistance in the circuit is R_S = 50 Ω. Voltage is dropped primarily across l_{SW} due to the narrowed constriction in the filament [2, 9, 10, 26, 28, 76]. As applied voltage V_A is increased to the point where V_{SW} = 2.5 V, the H_3O^+ energy level aligns with the Si-H-Si conduction band so that electrons are injected into the H_3O^+ defect by Fowler-Nordheim (F-N) tunneling, thus releasing a H^+ to form H_2O and initiating the RESET transition. As V_A continues to increase so that V_{SW} > 2.5 V, additional H_3O^+ defects align with the Si-H-Si conduction band so that electron injection transforms H_3O^+ into $H_2O + H^+$, where the H^+ then reacts with Si-H-Si to form $(SiH)_2$, as depicted in Figure 12 and in (1). In this way, a conductance gap with length l_{GAP} is formed within the switching region (Figure 10e) where l_{GAP} increases as V_A increases, thus accounting for the increasing device resistance as stop voltage increases (Figures 5c and 7).

The HRS band diagram shown in Figure 13b is drawn for the case where all defects in the switching region are converted into $(SiH)_2$ and $(SiOH)_2$ to form a conductance gap with length l_{GAP} ~ 5 nm. The $(SiH)_2$ defects have an

effective bandgap of 2.6 eV (Table II), leading to a discontinuity of ϕ_{HRS} in the CF conduction band (E_C). From Table II, ϕ_{HRS} in the range of 0.70 – 0.83 eV is calculated when considering the conduction band offsets between Si-H-Si and SiH+SiSi(5) relative to $(SiH)_2$, which is in reasonable agreement with the electron energy barrier of ~ 0.6 eV measured in the HRS [26].

The current in the HRS is typically orders of magnitude lower than in the LRS so that series resistance effects are negligible and the voltage drop across the gap is $V_{GAP} = V_A$. As shown in Figure 13b, when $V_{GAP} \geq 2.6$ V, the Fermi levels (E_F) in the portions of the CF on either side of the switching region become separated by 2.6 eV. This allows trap-assisted tunneling to occur where electrons are captured by the unoccupied charge-state in the $(SiH)_2$ conduction band (E_C) and electrons are emitted from the occupied charge-state in the $(SiH)_2$ valance band (E_V). During this electron/hole recombination process, some of 2.6 eV energy lost by the electron can be emitted as a photon, consistent with electroluminescence measurements made on HRS devices where a peak at 2.3 eV was observed [6]. As described above, the 2.6 eV bandgap of the $(SiH)_2$ defect leads to a HRS TAT threshold of ~ 2.6 V, which can explain the strong voltage dependence of the SET process and the SET threshold voltage at V_S ~ 2.5 V (see Figure 6).

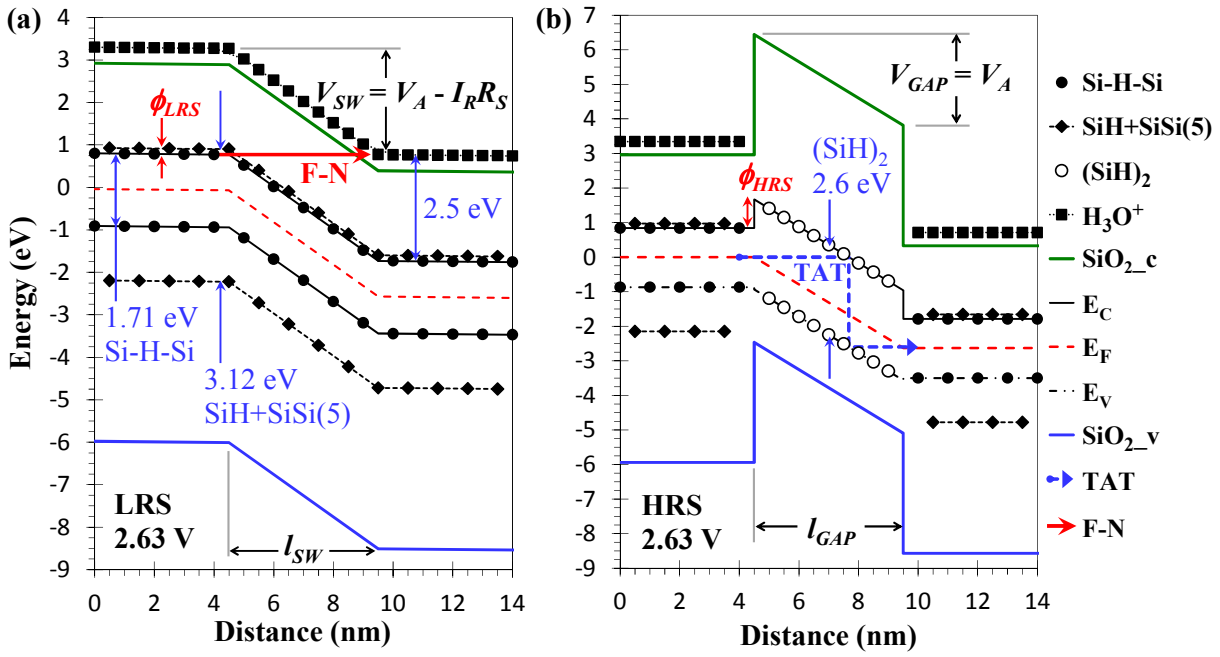

Figure 13. Energy band diagrams for: (a) LRS assuming R_S = 50 Ω and I_R = 2.63 mA, showing theoretical

bandgaps of Si-H-Si and SiH+SiSi(5), 2.5 eV offset of H_3O^+ energy level from Si-H-Si conduction band, switching region of length l_{SW} and F-N tunneling RESET transition; and (b) HRS showing theoretical bandgap of $(SiH)_2$ defect within gap region of length l_{GAP} and TAT SET transition. Both diagrams are drawn for applied voltage V_A = 2.63 V. The LRS and HRS electron energy barriers are ϕ_{LRS} and ϕ_{HRS}, respectively.

As shown in Figure 7b, SET transition voltage V_S is observed to be correlated with HRS resistance, where V_S increases from ~ 2.5 V to ~ 3.4 V in MIM devices as HRS resistance increases. This correlation has also been observed in unipolar HfO_2 RM devices and is well described by a cell-based percolation model of oxide breakdown with HRS resistance modeled as $R_{HRS} \propto \exp(l_{GAP}/l_0)$ consistent with electron tunneling, where l_0 is a characteristic gap length [55]. In SiO_2 RM devices, the V_S versus R_{HRS} trend may result from the current dependence of the H^+ desorption process. It is well-known that H^+ desorption from SiH depends on both voltage and current [98], where the current dependence is the result of electron-induced vibrational excitations of the Si-H bond [39, 46, 89]. As seen in Figure 13b, there is an asymmetry in the $(SiH)_2$ bandgap. From Table II, for $(SiH)_2$ the separation between E_C and E_{TH} is 0.74 eV larger than the separation between E_{TH} and E_V. As a result of this asymmetry, at 2.6 V there is a larger tunneling distance for electron capture by the $(SiH)_2$ defect as compared to the tunneling distance for electron emission from the defect. Since TAT current depends exponentially on tunneling distance [55, 99], a large l_{GAP} may lead to a TAT current that is too low to desorb H^+ at 2.6 V. In this case the voltage must increase to reduce the tunneling distance into the $(SiH)_2$ defect so that TAT current increases to the point where H^+ desorption can occur [26].

To provide deeper insights into the proposed RS mechanisms, future work plans include DFT calculations investigating proton uptake by absorbed water, $(SiOH)_2$, and the stability of the Si-H-Si/H_3O^+ complex. In addition, the stability of the $(SiH)_2$, $(SiOH)_2$, Si-H-Si, and Si_2=O-H_3O^+ defects in the presence of O_2 and H_2O should be verified using DFT calculations.

IV.E. Charge Transport Modeling

Modeling the *I-V* response can provide key information regarding the defects involved in charge transport and RS. Both hopping conduction and TAT have been used to successfully model charge transport in many different dielectric materials containing electron-trapping defects [100-105], and similar methods have been used to

characterize HfO_2 [8], $Ge_2Sb_2Te_5$ [104], TiO_2 [84] and SiO_x [5] RM materials where oxygen vacancies are often considered to be the trapping defects involved in charge transport and RS.

Previous investigations of SiO_2 RM materials have characterized the temperature dependence of device current, where the measured electron energy barriers were ~ 0.1 eV in the LRS and ~ 0.6 eV in the HRS [26]. As described above, these results are consistent with the energy barriers predicated by the theoretical electron energy band diagrams shown in Figure 13, and support the RS model given by (4) and shown in Figure 12. This previous work also found that hopping conduction accurately describes device current under low-bias conditions ≤ 1.5 V, where the non-Ohmic *I-V* response in the LRS and the decreasing device resistance with increasing temperature effectively eliminate the possibility of metallic conduction [26].

Figure 14 shows the LRS *I-V* response and charge transport modeling results that provide additional evidence supporting the proposed RS mechanisms. The voltage axis in Figure 14a was adjusted by subtracting $R_S \times I_{MEAS}$ from the applied voltage V_A in order to account for the voltage drop across the measured series resistance of R_S = 235 Ω in this MIM device (see Figure 1b), which enables the actual voltage V_{ADJ} across the CF to be determined. To investigate the low-voltage response ≤ 1.5 V, the LRS data were fit to the hopping conductance expression of the form

$$I_{HOP} = K \times V_{ADJ} \times \exp(LV_{ADJ}), \quad (5)$$

which is a form of hopping transport associated with Mott conduction [101]. The dashed curve in Figure 14a shows the results of the fit to (5), which yielded $I_{HOP} = 0.51V_{ADJ} \times \exp(0.23V_{ADJ})$ mA. In (5), parameter L = *qa/2dkT*, where *a* is the average hopping distance, *d* is the SiO_2 thickness, *k* is the Boltzmann constant, and *T* is the absolute temperature [26]. For L = 0.23, *d* = 60 nm and *T* = 298 K, plugging in the physical constants leads to an estimate of *a* = 0.7 nm for the average hopping distance. This corresponds to a defect density of ~ 3×10^{21} cm^{-3}, which is consistent with estimates made for HfO_2 RM materials [8], thus providing support for a LRS charge transport model based on hopping conduction. The hopping fit is observed to accurately model the measured data up to 1.5 V. However, the I_{MEAS} data begin to depart from the hopping expression above ~ 1.7 V, a phenomenon referred to as "overshoot" [26]. To investigate the overshoot region, I_{MEAS} data in the V_{ADJ} range from 2.2 to 2.7 V were fit using the F-N tunneling expression given by [26]

$$I_{FN} = I_{MEAS} - I_{HOP} = A \times V_{ADJ}^2 \times \exp(-B/V_{ADJ}). \quad (6)$$

As shown in Figure 14b, the fitting procedure yielded $I_{FN} = 66.8V_{ADJ}^2 \times \exp(-16.46/V_{ADJ})$ mA with an acceptable linear fit quality factor of $R^2 = 0.98$. These same data were also fit to the TAT expression given by [106, 107]

$$I_{TAT} = I_{MEAS} - I_{HOP} = I_o \times \exp(MV_{ADJ}^2), \quad (7)$$

which resulted in $I_{TAT} = 6.37\times10^{-3} \times \exp(0.71V_{ADJ}^2)$ mA with a good linear fit quality factor of $R^2 = 0.99$, as shown in Figure 14b. These results demonstrate that both the F-N and TAT expressions accurately fit the I_{MEAS} data in the overshoot region. An accurate fit to the F-N expression is often used to indicate TAT [108], and has been used to identify TAT as the active LRS current transport mechanism in Si-rich SiO_x RM devices [109]. Therefore, the results shown in Figure 14b indicate that both hopping conduction and TAT are present in the LRS. The I_{TAT} current component is plotted in Figure 14a as the dotted line. The resulting LRS charge transport model of $I_{MODEL} = I_{HOP} + I_{TAT}$ is plotted in Figure 14a as the solid line, which provides an accurate representation of the LRS *I-V* response up to the point where the RESET transition begins at $V_{ADJ} = 2.7$ V.

In order to further characterize the TAT overshoot region, a linear fit to the I_{MEAS} data from 2.2 to 2.7 V was made. The linear fit was extrapolated to the V_{ADJ} axis to estimate a TAT threshold voltage of $V_{TH} = 1.62$ V. This investigation was part of a larger study that characterized V_{TH} over a range of RESET stop voltages from 5 to 12 V, where $V_{TH} = 1.57 \pm 0.15$ V was found to be independent of stop voltage, indicating that the TAT overshoot phenomenon is a fundamental property of charge transport through the switching region [26]. The measured V_{TH} results and the assignment of TAT as the charge transport mechanism responsible for the overshoot phenomenon are consistent with electroluminescence measurements finding a peak energy of 1.6 eV in similar devices operating in the LRS, which was attributed to electron/hole recombination [6], as would be expected for TAT. The threshold of ~ 1.6 V indicates TAT through either Si*SiO(3) or Si-H-Si since these two defects have a bandgap energy of ~ 1.7 eV, very near the 1.6 V threshold (Table II). In the discussion above, the oxygen vacancy defect Si*SiO(3) was ruled-out as being involved in RS due to its instability in the presence O_2 and H_2O and the inability of an oxygen

vacancy creation/annihilation mechanism to explain the unipolar switching response. As a result, TAT through Si-H-Si is most likely responsible for the overshoot phenomenon, thus providing further support for the RS model.

It may be noted that TAT is an inelastic mechanism where a significant amount of energy is dissipated in a localized region around the electron-trapping defect [8]. This will lead to increased temperature within the switching region of the CF, which could be indistinguishable from the effects of Joule heating. Previous estimates indicate a localized temperature increase of ~ 130 degrees C within the CF for LRS measurements done at room temperature and 2 V bias [26]. The increased temperature due to TAT or Joule heating could help induce the RESET transition, which might support the argument that RESET in SiO_2 is a thermally-driven process [5, 15, 16]. However, the 130 degree C increase that we estimate for the CF in SiO_2 at 2 V bias is much lower than the increase of 400-500 degrees C estimated for NiO at ~ 0.4 V bias [2], suggesting that thermal energy may not be the dominant driver of the RESET process in SiO_2. Although the thermal dissolution process can adequately explain the stop voltage effect in some materials [2, 9, 26, 55, 77, 82, 83], it does not provide a ready explanation for the backward-scan effect that is only observed in SiO_x materials [18]. Furthermore, previous characterization data show that the RESET transition voltage *increases* as ambient temperature increases [110], and it has been demonstrated that the RESET process in SiO_2 materials has a strong voltage dependence with threshold of 2.46 V [54], both of which support a model where both thermal and voltage-dependent mechanisms may be involved. If TAT in the LRS were to continue unabated, the device might burn-out as a result of the large amount of energy deposited into the switching region. However, as shown in the band diagram of Figure 13a, F-N tunneling into H_3O^+ could initiate the RESET transition so that TAT through Si-H-Si defects ceases before burn-out can occur, thus providing a reasonable explanation for the self-compliant nature of SiO_2 RM devices.

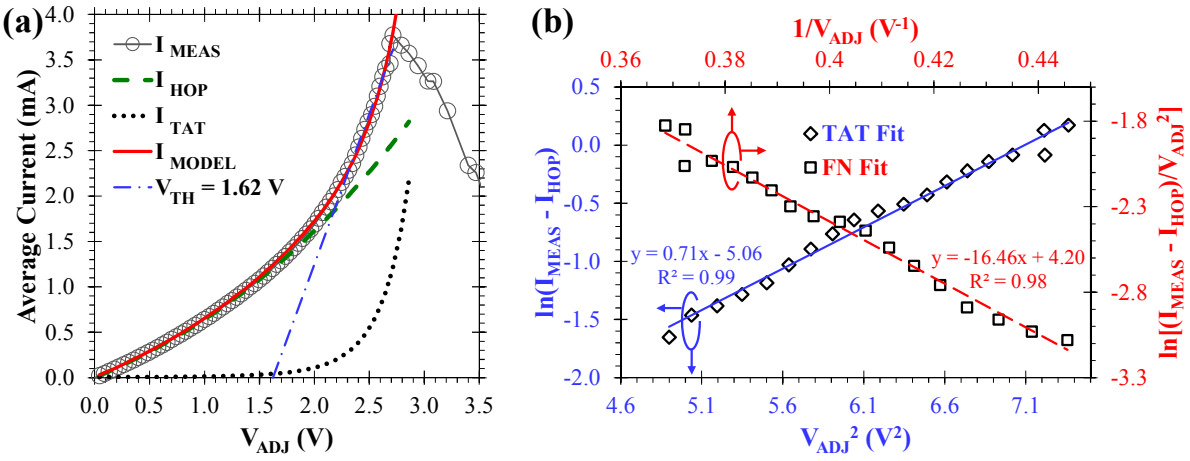

Figure 14. (a) Average measured current I_{MEAS} of ten 8V RESET sweeps versus adjusted voltage V_{ADJ}. The LRS was programed using a forward/reverse voltage sweep to 3.5 V. The applied voltage V_A was adjusted to account for the voltage drop across the series resistance of R_S = 235 Ω using $V_{ADJ} = V_A - I_{MEAS} \times R_S$. The I_{MEAS} data are fit to the hopping formula from 0 – 1.5 V to obtain I_{HOP} (dashed line). A linear fit to the I_{MEAS} data in the voltage range from 2.2 to 2.7 V (dash-dot line) estimates the overshoot threshold voltage V_{TH} = 1.62 V. The TAT current component I_{TAT} (dotted line) in (a) is obtained from the linear fit to a plot of $\ln(I_{MEAS} - I_{HOP})$ versus V_{ADJ}^2 shown in (b). The linear fit to a plot of $\ln[(I_{MEAS} - I_{HOP})/V_{ADJ}^2]$ versus $1/V_{ADJ}^2$ in (b) confirms that F-N tunneling also fits the I_{MEAS} data in the overshoot region. The solid line in (a) shows the LRS current model: $I_{MODEL} = I_{HOP} + I_{TAT}$.

In fact, the electroforming and RS models developed herein provide natural explanations for many of the unusual characteristics of the SiO_2-based RM device, including the self-compliant *I-V* response as noted directly above. The stop voltage effect is naturally explained by F-N tunneling controlling the RESET process (Figure 13a), where the conductance gap formed in the switching region (Figure 10e) is a direct function of the stop voltage applied during RESET, leading to a device resistance that increases with stop voltage (Figures 5c and 7). The backward-scan effect is not observed in other RM materials, and is explained here by the voltage-dependent SET and RESET mechanisms. The lower electroforming voltage achieved after reducing anneal (Figure 2) is explained by the reaction of H_2 with as-deposited Si-Si defects to form $(SiH)_2$, where charging of the $(SiH)_2$ defect causes H desorption to directly form Si-H-Si in a low-energy process. The RS model based on water-related defects readily explains why the CF forms very near the sidewall surface (in sidewall devices), and why only highly porous e-beam

oxides (with potentially high water content) can be electroformed in bulk device architectures (Figure 4). The robust nonvolatility in air for bias < 2 V is explained by H- and OH-passivation of the defects involved in RS (Figure 12), where this passivation is temporarily lost during a switching event so that RS fails in ambients containing O_2 due to oxidation of the un-passivated defects (Figure 8). Finally, the unusual unipolar switching characteristic where $V_S \leq V_R$ is explained directly by the RS model where H^+ desorption from $(SiH)_2$ induces the SET transition and F-N tunneling into the H_3O^+ defect releases a H^+ to induce the RESET transition (Figures 12 and 13). Each of these explanations are supported by the wealth of information available in the technical literature regarding defects in silicon oxide materials. The results presented herein make it clear that the SiO_2 RM device provides an exceptional platform for the study of SiO_2 defects, which may lead to better understanding of breakdown and degradation mechanisms in MOS devices.

V. Conclusions

Electroforming and resistive switching in amorphous SiO_2 materials were investigated using experiments controlling anneal temperature, etch time and operating ambient. Thermal anneal in reducing ambient lowered electroforming voltage by over 50 % to < 10 V, and identified the $(SiH)_2$ defect as a potential electroformation precursor. Conductive filaments were found to form within ~ 4 nm of the sidewall surface in devices with an etched SiO_2 layer, whereas most filaments are > 10 nm from the electrode edge in bulk devices having a continuous SiO_2 layer. Resistive switching of unpassivated devices failed at 1 atm pressure in both air and pure O_2/N_2, although switching was recovered after placing the devices back under vacuum. Attempts to operate devices in 1 atm of air led to vacuum switching recovery at ~ 9.5 V, whereas vacuum switching was recovered at ~ 4.6 V after operating attempts in 1 atm of pure O_2/N_2, indicating that H_2O in the air has a more pronounced effect on resistive switching as compared to O_2 alone. Incorporating a hermetic passivation layer enabled successful reversible switching in 1 atm air. Defect energetics, oxide degradation mechanisms and electrochemical reactions in SiO_2 were discussed in relation to electroforming and resistive switching, leading to a localized resistive switching model involving proton exchange reactions given by $(SiH)_2 + (SiOH)_2 \leftrightarrow$ Si-H-Si + Si_2=O-H_3O^+. The energy of H^+ desorption from the $(SiH)_2$ defect was found to be consistent with the SET transition at ~ 2.5 V in the current-voltage response. The RESET transition was attributed to Fowler-Nordheim tunneling into the positive-charged H_3O^+ defect, although it was noted that thermal energy due to inelastic tunneling through the Si-H-Si defect could also play a role. Electron

energy band diagrams were constructed using mono-energetic defect energy levels based on density functional theory calculations. Band diagrams for both the LRS and HRS were found to be consistent with measured electron energy barriers and electroluminescence results reported for similar devices. Supporting evidence for the resistive switching model was provided in the form of low-frequency noise measurements indicating a $1/f$ signature in the LRS and $1/f^2$ noise in the HRS, consistent with charge transport through electron-trapping defects. Low-resistance state current fit well to hopping conduction at low bias ≤ 1.5 V. A current overshoot phenomenon with threshold near 1.6 V was found to be consistent with trap-assisted tunneling through the Si-H-Si defect, as well as reported electroluminescence at 1.6 eV peak energy. Although perhaps other defect combinations can explain device performance, the models developed herein provide reasonable and accurate explanations of electroforming and resistive switching in SiO_2-based memory devices. Overall, the results demonstrate that the SiO_2-based device provides a good experimental platform to study amorphous SiO_2 defects, which may lead to better understanding of MOS device breakdown and degradation mechanisms. The described electroforming methods, conditioning techniques and operating models are potentially useful for development of SiO_2-based resistive memory devices for future nonvolatile memory products.

VI. Acknowledgements

This material is based upon work supported by the National Science Foundation under Grant No. IIP-1127537 and the U.S. Navy under Small Business Innovation Research Contract No. N66001-11-C-5212. We are grateful to Tronics MEMS Inc., Richardson, TX, for fabricating the MIM crossbar devices used in this work.

VII. References

[1] R. Waser and M. Aono, "Nanoionics-based resistive switching memories," *Nat. Mater*., 2007, **6**, 833 – 840; DOI: 10.1038/nmat2023

[2] S. Long, C. Cagli, D. Ielmini, M. Liu, and J. Sune, "Analysis and modeling of resistive switching statistics," *J. Appl, Phys*., 2012, **111**, 074508; DOI: 10.1063/1.3699369

[3] C. Park, S. H. Jeon, S. C. Chae, S. Han, B. H. Park, S. Seo, and D.-W. Kim, "Role of structural defects in the unipolar resistive switching characteristics of Pt/NiO/Pt structures," *Appl. Phys. Lett*., 2008, **93**, 042102; DOI: 10.1063/1.2963983

[4] D. S. Jeong, R. Thomas, R. S. Katiyar, J. F. Scott, H. Kohlstedt, A. Petraru and C. S. Hwang, "Emerging memories: resistive switching mechanisms and current status," *Reports on Progress in Physics*, 2012, **75**, 076502; DOI: 10.1088/0034-4885/75/7/076502

[5] A. Mehonic, S. Cueff, M. Wojdak, S. Hudziak, O. Jambois, C. Labbe, B. Garrido, R. Rizk, and A. J. Kenyon, "Resistive switching in silicon suboxide films," *J. Appl. Phys*., 2012, **111**, 074507; DOI: 10.1063/1.3701581

[6] C. He, J. Li, X. Wu, P. Chen, J. Zhao, K. Yin, M. Cheng, W. Yang, G. Xie, D. Wang, D. Liu, R. Yang, D. Shi, Z. Li, L. Sun, and G. Zhang, "Tunable Electroluminescence in Planar Graphene/SiO_2 Memristors," *Adv. Mater*., 2013, **25**, 5593-5598; DOI: 10.1002/adma.201302447

[7] J. Yao, L. Zhong, D. Natelson, and J. M. Tour, "In situ imaging of the conducting filament in a silicon oxide switch," *Sci. Rep*., 2012, **2**, 242-1 – 242-5; DOI: 10.1038/srep00242

[8] G. Bersuker, D. C. Gilmer, D. Veksler, P. Kirsch, L. Vandelli, A. Padovani, L. Larcher, K. McKenna, A. Shluger, V. Iglesias, M. Porti, and M. Nafria, "Metal oxide resistive memory switching mechanism based on conductive filament properties," *J. Appl. Phys*., 2011, **110**, 124518-1–124518-12; DOI: 10.1063/1.3671565

[9] S. Long, L. Perniola, C. Cagli, J. Buckley, X. Lian, E. Miranda, F. Pan, M. Liu, and J. Sune, "Voltage and Power-Controlled Regimes in the Progressive Unipolar RESET Transition of HfO_2-Based RRAM," *Sci. Rep.*, 2013, **3**, 2929; DOI: 10.1038/srep02929

[10] A. Belmonte, R. Degraeve, A. Fantini, W. Kim, M. Houssa, M. Jurczak, and L. Goux, "Origin of the current discretization in deep reset states of an Al_2O_3/Cu-based conductive-bridging memory, and impact on state level and variability," *Appl. Phys. Lett*., 2014, **104**, 233508-1 – 233508-4; DOI: 10.1063/1.4883856

[11] Y. Wang, K. Chen, X. Qian, Z. Fang, W. Li, and J. Xu, "The x dependent two kinds of resistive switching behaviors in SiOx films with different x component," *Appl. Phys. Lett*., 2014, **104**, 012112-1 – 012112-4; DOI: 10.1063/1.4861592

[12] J. Yao, L. Zhong, D. Natelson, and J. M. Tour, "Etching-dependent reproducible memory switching in vertical SiO_2 structures," *Appl. Phys. Lett*., 2008, **93**, 253101; DOI: 10.1063/1.3045951

[13] J. Yao, L. Zhong, Z. Zhang, T. He, Z. Jin, P. J. Wheeler, D. Natelson, and J. M. Tour, "Resistive Switching in Nanogap Systems on SiO_2 Substrates," *Small*, 2009, **5**, 2910–2915; DOI: 10.1002/smll.200901100

[14] Y. Wang, Y.-T. Chen, F. Xue, F. Zhou, Y.-F. Chang, B. Fowler and J. C. Lee, "Memory switching properties of e-beam evaporated SiOx on N++ Si substrate," *Appl. Phys. Lett*., 2012, **100**, 083502-1 – 083502-3; DOI: 10.1063/1.3687724

[15] J. Yao, J. Lin, Y. Dai, G. Ruan, Z. Yan, L. Li, L. Zhong, D. Natelson, and J. M. Tour, "Highly transparent nonvolatile resistive memory devices from silicon oxide and graphene," *Nature Communications*, 2012, **3**, 1-8; DOI:10.1038/ncomms2110

[16] J. Yao, Z. Sun, L. Zhong, D. Natelson and J. M. Tour, "Resistive Switches and Memories from Silicon Oxide," *Nano Letters*, 2010, **10**, 4105–4110; DOI: 10.1021/nl102255r

[17] L. Ji, Y. F. Chang, B. Fowler, Y. C. Chen, T. M. Tsai, K. C. Chang, M. C. Chen, T. C. Chang, S. M. Sze, E. T. Yu, and J. C. Lee, "Integrated One Diode−One Resistor Architecture in Nanopillar SiO_x Resistive Switching Memory by Nanosphere Lithography," *Nano Lett*., 2013, **14**, 813 – 818; DOI: 10.1021/nl404160u

[18] Y.-F. Chang, L. Ji, Y. Wang, P.-Y. Chen, F. Zhou, F. Xue, B. Fowler, E.T. Yu, and J. C. Lee, "Investigation of edge- and bulk-related resistive switching behaviors and backward-scan effects in SiO_x-based resistive switching memory," *Appl. Phys. Lett*., 2013, **103**, 193508-1 – 193508-4; DOI: 10.1063/1.4829526

[19] Y. Wang, B. Fowler, F. Zhou, Y.-F. Chang, Y.-T. Chen, F. Xue, and J.C. Lee, "Effects of sidewall etching on electrical properties of SiOx resistive random access memory," *Appl. Phys. Lett*., 2013, **103**, 213505-1 – 213505-4; DOI: 10.1063/1.4832595

[20] Y.-F. Chang, P.-Y. Chen, B. Fowler, Y.-T. Chen, F. Xue, Y. Wang, F. Zhou, and J. C. Lee, "Understanding the resistive switching characteristics and mechanism in active SiO_x-based resistive switching memory," *J. Appl. Phys*., 2012, **112**, 123702-1–123702-8; DOI: 10.1063/1.4769218

[21] J. Yao, L. Zhong, D. Natelson, and J. M. Tour, "Intrinsic resistive switching and memory effects in silicon oxide," *Appl. Phys. A*, 2011, **102**, 835–839; DOI: 10.1007/s00339-011-6267-6

[22] Y.-F. Chang, B. Fowler, Y.-C. Chen, Y.-T. Chen, Y. Wang, F. Xue, F. Zhou, and J. C. Lee, "Intrinsic SiOx-based unipolar resistive switching memory. I. Oxide stoichiometry effects on reversible switching and program window optimization," *J. Appl. Phys.*, 2014, **116**, 043708-1 – 043708-10; DOI: 10.1063/1.4891242

[23] Y.-T. Chen, B. Fowler, Y. Wang, F. Xue, F. Zhou, Y.-F. Chang, P.-Y. Chen, and J. C. Lee, "Tristate Operation in Resistive Switching of SiO_2 Thin Films," *IEEE Electron Device Lett*., 2012, **33**, 1702-1704; DOI: 10.1109/LED.2012.2218566

[24] Y.-F. Chang, L. Ji, Z.-J. Wu, F. Zhou, Y. Wang, F. Xue, B. Fowler, E. T. Yu, P. S. Ho, and J. C. Lee, "Oxygen-induced bi-modal failure phenomenon in SiO_x-based resistive switching memory," *Appl. Phys. Lett*., 2013, **103**, 033521; DOI: 10.1063/1.4816162

[25] Y. Wang, B. Fowler, Y.-T. Chen, F. Xue, F. Zhou, Y.-F. Chang, and J. C. Lee, "Effect of hydrogen/deuterium incorporation on properties of resistive random access memory with SiO_x," *Appl. Phys. Lett*., 2012, **101**, 183505; DOI: 10.1063/1.4765356

[26] Y.-F. Chang, B. Fowler, Y.-C. Chen, Y.-T. Chen, Y. Wang, F. Xue, F. Zhou, and J. C. Lee, "Intrinsic SiOx-based unipolar resistive switching memory. II. Thermal effects on charge transport and characterization of multilevel programing," *J. Appl. Phys.*, 2014, **116**, 043709-1 – 043709-12; DOI: 10.1063/1.4891244

[27] F. Zhou, Y.-F. Chang, Y. Wang, Y.-T. Chen, F. Xue, B. W. Fowler, and J. C. Lee, "Discussion on device structures and hermetic encapsulation for SiO_x random access memory operation in air," *Appl. Phys. Lett*., 2014, **105**, 163506-1 – 163506-4; DOI: 10.1063/1.4900422.

[28] E. Miranda and J. Suñé, "Analytic Modeling of Leakage Current Through Multiple Breakdown Paths in SiO_2 Films," *IEEE International Reliability Physics Symposium*, 2001, 367-379

[29] E. Wu, J. Suñé, W. Lai, A Vayshenker and D. Harmon, "A Comprehensive Investigation of Gate Oxide Breakdown of P+Poly/PFETs Under Inversion Mode," *IEEE-IEDM Technical Digest*, 2005, 396-399; DOI: 10.1109/IEDM.2005.1609361

[30] Y.-T. Chen, B. Fowler, Y. Wang, F. Xue, F. Zhou, Y.-F. Chang, and J. C. Lee, "Random Process of Filamentary Growth and Localized Switching Mechanism in Resistive Switching of SiO_x Thin Films," *ECS J. Solid State Sci. Technol*., 2012, **1**, P148-P151; DOI: 10.1149/2.013203jss

[31] E. H. Poindexter, "Chemical reactions of hydrogenous species in the Si/SiO_2 system," *Journal of Non-Crystalline Solids*, 1995, **187**, 257-263

[32] C. R. Helms and E. H. Poindexter, "The silicon-silicon-dioxide system: its microstructure and imperfections," *Rep. Prog. Phys*., 1994, **57**, 791-852

[33] R. B. Comizzoli, "Bulk and Surface Conduction in CVD SiO_2 and PSG Passivation Layers," *ECS J. Solid State Sci. Technol*., 1976, **123**, 386 – 391

[34] I. G. Batyrev, B. Tuttle, D. M. Fleetwood, R. D. Schrimpf, L. Tsetseris, and S. T. Pantelides "Reactions of Water Molecules in Silica-Based Network Glasses," *Phys. Rev. Lett*., 2008, **100**, 105503; DOI: 10.1103/PhysRevLett.100.105503

[35] T. S. Mahadevan and S. H. Garofalini, "Dissociative Chemisorption of Water onto Silica Surfaces and Formation of Hydronium Ions," *J. Phys. Chem. C*, 2008, **112**, 1507-1515; DOI: 10.1021/jp076936c

[36] I. G. Batyrev, M. P. Rodgers, D. M. Fleetwood, R. D. Schrimpf, and S. T. Pantelides, "Effects of Water on the Aging and Radiation Response of MOS Devices," *IEEE Transactions on Nuclear Science*, 2006, **53**, 3629-3635; DOI: 10.1109/TNS.2006.884787

[37] Z. A. Weinberg, D. R. Young, J. A. Calise, S. A. Cohen, J. C. DeLuca, and V. R. Deline, "Reduction of electron and hole trapping in SiO_2 by rapid thermal annealing," *Appl. Phys. Lett*., 1984, **45**, 1204-1206; DOI: 10.1063/1.95098

[38] D.-K. Kim, W. D. Nix, R. P. Vinci, M. D. Deal, and J. D. Plummer, "Study of the effect of grain boundary migration on hillock formation in Al thin films," *J. Appl. Phys*., 2001, **90**, 781; DOI: 10.1063/1.1381045

[39] B. Tuttle and C. G. Van de Walle, "Structure, energetics, and vibrational properties of Si-H bond dissociation in silicon," *Physical Review B*, 1999, **59**, 884 – 889; DOI: 10.1103/PhysRevB.59.12884

[40] R. J. Milanowski, M. P. Pagey, A. I. Matta, B. L. Bhuva, L. W. Massengill, and S. E. Kerns, "Combined Effect of X-Irradiation and Forming Gas Anneal on the Hot-Carrier Response of MOS Oxides," *IEEE Trans. Nucl. Sci*., 1993, **40**, 1360-1366; DOI: 10.1109/23.273531

[41] M. P. Pagey, R. J. Milanowski, K. T. Henegar, B. L. Bhuva, and S. E. Kerns, "Comparison of Forming Gas, Nitrogen, and Vacuum Anneal Effects," *IEEE Trans. Nucl. Sci*., 1995, **42**, 1758-1763; DOI: 10.1109/23.488776

[42] G. Pacchioni and G. Ierano, "Ab initio theory of optical transitions of point defects in SiO_2," *Phys. Rev. B*, 1998, **57**, 818–832

[43] P. E. Blöchl, "First-principles calculations of defects in oxygen-deficient silica exposed to hydrogen," *Phys. Rev. B*, 2000, **62**, 6158-6179; DOI: 10.1103/PhysRevB.62.6158

[44] H.-D. Lin and D.-C. Ho, "Detection of pinhole defects on chips and wafers using DCT enhancement in computer vision systems," *Int. J. Adv. Manuf. Technol*., 2007, **34**, 567–583; DOI: 10.1007/s00170-006-0614-3

[45] T. Bakos, S. N. Rashkeev, and S. T. Pantelides, "Reactions and Diffusion of Water and Oxygen Molecules in Amorphous SiO_2," *Phys. Rev. Lett.*, 2002, **88**, 055508-1 – 055508-4; DOI: 10.1103/PhysRevLett.88.055508

[46] J. Suñé and E. Wu, "Mechanisms of hydrogen release in the breakdown of SiO_2-based gate oxides," *IEEE-IEDM Technical Digest*, 2005, 388-391; DOI: 10.1109/IEDM.2005.1609359

[47] N. Lifshitz and G. Smolinsky, "Detection of water-related charge in electronic dielectrics," *Appl. Phys. Lett*., 1989, **55**, 408-410; DOI: 10.1063/1.101570

[48] L. Tsetseris, X. Zhou, D. M. Fleetwood, R. D. Schrimpf, and S. T. Pantelides, "Field-induced reactions of water molecules at Si-dielectric interfaces," *Mat. Res. Soc. Symp. Proc*., 2004, **786**, E3.3.1

[49] S. T. Pantelides, S. N. Rashkeev, R. Buczko, D. M. Fleetwood, and R. D. Schrimpf, "Reactions of Hydrogen with Si-SiO_2 Interfaces," *IEEE Trans. Nucl. Sci*., 2000, **47**, 2262-2268; DOI: 10.1109/23.903763

[50] J. Suñé and E. Wu, "A New Quantitative Hydrogen-Based Model for Ultra-Thin Oxide Breakdown," *Symposium on VLSI Technology Digest of Technical Papers*, 2001, 97

[51] K. H. Beckmann and N. J. Harrick, "Hydrides and Hydroxyls in Thin Silicon Dioxide Films," *J. Electrochem. Soc*., 1971, **118**, 614-619

[52] S. T. Pantelides, L. Tsetseris, S. N. Rashkeev, X. J. Zhou, D. M. Fleetwood, R. D. Schrimpf, "Hydrogen in MOSFETs – A primary agent of reliability issues," *Microelectronics Reliability*, 2007, **47**, 903–911; DOI: 10.1016/j.microrel.2006.10.011

[53] S. T. Pantelides, L. Tsetseris, M. J. Beck, S. N. Rashkeev, G. Hadjisavvas, I. G. Batyrev, B. R. Tuttle, A. G. Marinopoulos, X. J. Zhou, D. M. Fleetwood, R. D. Schrimpf, "Performance, reliability, radiation effects, and aging issues in microelectronics – From atomic-scale physics to engineering-level modeling," *Solid-State Electronics*, 2010, **54**, 841–848; DOI: 10.1016/j.sse.2010.04.041

[54] F. Zhou, Y.-F. Chang, K. Byun, B. Fowler, and J. C. Lee, "Characterization of external resistance effect and performance optimization in unipolar-type SiO_x-based resistive switching memory," *Appl. Phys. Lett*., 2014, **105**, 133501-1 – 133501-4; DOI: 10.1063/1.4896877

[55] S. Long, X. Lian, C. Cagli, L. Perniola, E. Miranda, M. Liu, and J. Suñé, "A Model for the Set Statistics of RRAM Inspired in the Percolation Model of Oxide Breakdown," *IEEE Elect. Dev. Lett*., 2013, **34**, 999; DOI: 10.1109/LED.2013.2266332

[56] Y. Wang, X. Qian, K. Chen, Z. Fang, W. Li, and J. Xu, "Resistive switching mechanism in silicon highly rich SiOx (x < 0.75) films based on silicon dangling bonds percolation model," *Appl. Phys. Lett*., 2013, **102**, 042103-1 – 042103-5; DOI: 10.1063/1.4776695

[57] V. Atluri, N. Herbots, D. Dagel, S. Bhagvat, S. Whaley, "Hydrogen passivation of Si(100) wafers as templates for low temperature (T < 600°C) epitaxy," *Nuclear Instruments and Methods in Physics Research B*, 1996, **118**, 144 – 150

[58] Y. J. Chabal, G. S. Higashi, and K. Raghavachari, "Infrared spectroscopy of Si(111) and Si(100) surfaces after HF treatment: Hydrogen termination and surface morphology," *J. Vac. Sci. Technol. A*, 1989, **7**, 2104 – 2109; DOI: 10.1116/1.575980

[59] P. D. Welch, "Use of fast Fourier transform for estimation of power spectra: A method based on time averaging over short, modified periodograms," *IEEE Trans. Audio Electroacoust*., 1967, **AU-15**, 70-73

[60] N. K. Rajan, D. A. Routenberg, J. Chen, and M. A. Reed, "1/f Noise of Silicon Nanowire BioFETs," *IEEE Elect. Dev. Lett*., 2010, **31**, 615-617; DOI: 10.1109/LED.2010.2047000

[61] S. Yu, R. Jeyasingh, Y. Wu, and H.-S. P. Wong, "Understanding the Conduction and Switching Mechanism of Metal Oxide RRAM through Low Frequency Noise and AC Conductance Measurement and Analysis," IEEE International Electron Devices Meeting (IEDM), 2011, 12.1.1 - 12.1.4; DOI: 10.1109/IEDM.2011.6131537

[62] F. M. Puglisi, L. Larcher, G. Bersuker, A. Padovani, and P. Pavan, "An Empirical Model for RRAM Resistance in Low- and High-Resistance States," *IEEE Elect. Dev. Lett*., 2013, **34**, 387-389; DOI: 10.1109/LED.2013.2238883

[63] T. Grasser, B. Kaczer, W. Goes, H. Reisinger, T. Aichinger, P. Hehenberger, P.-J. Wagner, F. Schanovsky, J. Franco, M. T. Luque, and M. Nelhiebel, "The Paradigm Shift in Understanding the Bias Temperature Instability: From Reaction–Diffusion to Switching Oxide Traps," *IEEE Transactions on Electron Devices*, 2011, **58**, 3652-3666; DOI: 10.1109/TED.2011.2164543

[64] W. Goes, F. Schanovsky, T. Grasser, H. Reisinger, and B. Kaczer, "Advanced Modeling of Oxide Defects for Random Telegraph Noise," *IEEE 21st International Conference on Noise and Fluctuations*, 2011, 204-207

[65] F. Crupi, G. Giusi, G. Iannaccone, P. Magnone, C. Pace, E. Simoen, and C. Claeys, "Analytical model for the 1/f noise in the tunneling current through metal-oxide-semiconductor structures," *Journal of Applied Physics*, 2009, **106**, 073710; DOI: 10.1063/1.3236637

[66] S. Lombardo, J. H. Stathis, B. P. Linder, K. L. Pey, F. Palumbo, and C. H. Tung, "Dielectric breakdown mechanisms in gate oxides," *J. Appl. Phys.*, 2005, **98**, 121301; DOI: 10.1063/1.2147714

[67] E. Wu, J. Suñé and R.-P. Vollertsen, "Comprehensive physics-based breakdown model for reliability assessment of oxides with thickness ranging from 1 nm up to 12 nm," *IEEE International Reliability Physics Symposium*, 2009, 708-717; DOI: 10.1109/IRPS.2009.5173335

[68] Y.-F. Wang, X.-Y. Qian, K.-J. Chen, Z.-H. Fang, W. Li, J. Xu , "Fabrication of Silicon Highly-rich SiOx (x<0.75) and Its Novel Resistive Switching Behaviors," *IEEE 11th International Conference on Solid-State and Integrated Circuit Technology (ICSICT)*, 2012, 1 – 3; DOI: 10.1109/ICSICT.2012.6467606

[69] P. E. Bunson, M. Di Ventra, S. T. Pantelides, D. M. Fleetwood, and R. D. Schrimpf, "Hydrogen-Related Defects in Irradiated SiO_2," *IEEE Transactions on Nuclear Science*, 2000, **47**, 2289 – 2295; DOI: 10.1109/23.903767

[70] P. E. Blöchl and J. H. Stathis, "Hydrogen Electrochemistry and Stress-Induced Leakage Current in Silica," *Physical Review Letters*, 1999, **83**, 372-375; DOI: 10.1103/PhysRevLett.83.372

[71] Y. Mitani, H. Satake and A. Toriumi, "Experimental Evidence of Hydrogen-Related SILC Generation in Thin Gate Oxide," *IEEE International Electron Devices Meeting Technical Digest*, 2001, 129-132

[72] J. Suñé, "New Physics-Based Analytic Approach to the Thin-Oxide Breakdown Statistics," *IEEE Electron Device Letters*, 2001, **22**, 296-298

[73] J. Suñé, E. Miranda, M. Nafria and X. Aymerich, "Point Contact Conduction at the Oxide Breakdown of MOS Devices," *IEEE-IEDM Tech. Dig*., 1998, 191–194

[74] A. Cester, L. Bandiera, J. Suñé, L. Boschiero, G. Ghidini and A. Paccagnella, "A Novel Approach to Quantum Point Contact for post Soft Breakdown Conduction," *IEEE-IEDM Tech. Dig*., 2001, 632-635

[75] W.-C. Luo, J.-C. Liu, Y.-C. Lin, C.-L. Lo, J.-J. Huang, K.-L. Lin, and T.-H. Hou, "Statistical Model and Rapid Prediction of RRAM SET Speed–Disturb Dilemma," *IEEE Trans. Elect. Dev.*, 2013, **60**, 3760; DOI: 10.1109/TED.2013.2281991

[76] E. A. Miranda, C. Walczyk, C. Wenger, and T. Schroeder, "Model for the Resistive Switching Effect in HfO_2 MIM Structures Based on the Transmission Properties of Narrow Constrictions," *IEEE Elect. Dev. Lett.*, 2010, **31**, 609; DOI: 10.1109/LED.2010.2046310

[77] S. Long, X. Lian, C. Cagli, X. Cartoixa R. Rurali, E. Miranda, D. Jimenez, L. Perniola, M. Liu, and J. Sune, "Quantum-size effects in hafnium-oxide resistive switching," *Appl. Phys. Lett.*, 2013, **102**, 183505; DOI: 10.1063/1.4802265

[78] P. E. Blöchl and J. H. Stathis, "Aspects of Defects in Silica Related to Dielectric Breakdown of Gate Oxides in MOSFETs," *Physica B*, 1999, **273-274**, 1022 – 1026; DOI: 10.1016/S0921-4526(99)00628-6

[79] J. Robertson, "Intrinsic defects and hydroxyl groups in a-SiO_2," *J. Phys. C: Solid State Phys*., 1984, **17**, L221-L225

[80] W. Goes and T. Grasser, "Charging and discharging of oxide defects in reliability issues," *IEEE International Integrated Reliability Workshop Final Report*, 2007, 27-32; DOI: 10.1109/IRWS.2007.4469216

[81] Z.-Yi Lu, C. J. Nicklaw, D. M. Fleetwood, R. D. Schrimpf, and S. T. Pantelides, "Structure, Properties, and Dynamics of Oxygen Vacancies in Amorphous SiO_2," *Physical Review Letters*, 2002, **89**, 285505-1 – 285505-4; DOI: 10.1103/PhysRevLett.89.285505

[82] S. Long, X. Lian, T. Ye, C. Cagli, L. Perniola, E. Miranda, M. Liu, and J. Suñé, "Cycle-to-Cycle Intrinsic RESET Statistics in HfO_2-Based Unipolar RRAM Devices," *IEEE Elect. Dev. Lett*., 2013, **34**, 623; DOI: 10.1109/LED.2013.2251314

[83] S. Long, C. Cagli, D. Ielmini, M. Liu, and J. Suñé, "Reset Statistics of NiO-Based Resistive Switching Memories," *IEEE Elect. Dev. Lett*., 2011, **32**, 1570; DOI: 10.1109/LED.2011.2163613

[84] M. D. Pickett, D. B. Strukov, J. L. Borghetti, J. J. Yang, G. S. Snider, D. R. Stewart, and R. S. Williams, "Switching dynamics in titanium dioxide memristive devices," *J. Appl. Phys*., 2009, **106**, 074508-1 – 074508-6; DOI: 10.1063/1.3236506

[85] S. Kvatinsky, E. G. Friedman, A. Kolodny, and U. C. Weiser, "TEAM: ThrEshold Adaptive Memristor Model," *IEEE Transactions on Circuits and Systems I: Regular Papers*, 2013, **60**, 211-221; DOI: 10.1109/TCSI.2012.2215714

[86] B. Gao, S. Yu, N. Xu, L.F. Liu, B. Sun, X.Y. Liu, R.Q. Han, J.F. Kang, B. Yu, Y.Y. Wang, "Oxide Based RRAM Switching Mechanism: A New Ion-Transport-Recombination Model," *IEEE IEDM Tech. Dig*., 2008, 1-4; DOI: 10.1109/IEDM.2008.4796751

[87] J. H. Stathis, "Dissociation kinetics of hydrogen-passivated (100) Si/SiO_2 interface defects," *J. Appl. Phys*., 1995, **77**, 6205 – 6207; DOI: 10.1063/1.359148

[88] S. M. Myers, D. M. Follstaedt, H. J. Stein, and W. R. Wampler, "Deuterium bonding at internal surfaces in silicon," *Phys. Rev. B*, 1992, **45**, 3914-3917

[89] K. Hess, B. Tuttle, F. Register, and D. K. Ferry, "Magnitude of the threshold energy for hot electron damage in metal–oxide–semiconductor field effect transistors by hydrogen desorption," *Appl. Phys. Lett*., 1999, **75**, 3147-3149

[90] F. A. Cotton and G. Wilkinson, "Advanced Inorganic Chemistry," pp. 163-168, Interscience, New York (1972)

[91] P. Ayotte, M. Hébert, P. Marchand, "Why is hydrofluoric acid a weak acid?" *J. Chem. Phys*., 2005, **123**, 184501; DOI: 10.1063/1.2090259

[92] G. J. Gerardi, E. H. Poindexter, P. J. Caplan, M. Harmatz, W. R. Buchwald and N. M. Johnson, "Generation of P_b Centers by High Electric Fields: Thermochemical Effects," *J. Electrochem. Soc*., 1989, **136**, 2609-2614; DOI: 10.1149/1.2097511

[93] C. E. Blat, E. H. Nicollian, and E. H. Poindexter, "Mechanism of negative-bias-temperature instability," *J. Appl. Phys*., 1991, **69**, 1712-1720; DOI: 10.1063/1.347217

[94] D.-S. Shang, L. Shi, J.-R. Sun and B.-G. Shen, "Local resistance switching at grain and grain boundary surfaces of polycrystalline tungsten oxide films," *Nanotechnology*, 2011, **22**, 254008; DOI: 10.1088/0957-4484/22/25/254008

[95] S. G. Park, B. Magyari-Köpe, and Y. Nishi, "Theoretical Study of the Resistance Switching Mechanism in Rutile TiO_{2-x} for ReRAM: the role of oxygen vacancies and hydrogen impurities," *Symposium on VLSI Technology Digest of Technical Papers*, 2001, 46-47

[96] L. C. T. Shoute, N. Pekas, Y. Wu and R. L. McCreery, "Redox driven conductance changes for resistive memory," *Appl. Phys. A*, 2011, **102**, 841–850

[97] T. Bakos, S. N. Rashkeev, and S. T. Pantelides, "H_2O and O_2 molecules in amorphous SiO_2: Defect formation and annihilation mechanisms," *Phys. Rev. B*, 2004, **69**, 195206-1 – 195206-9; DOI: 10.1103/PhysRevB.69.195206

[98] K. Hess, I. C. Kizilyalli, and J. W. Lyding, "Giant Isotope Effect in Hot Electron Degradation of Metal Oxide Silicon Devices," *IEEE Trans. Elect. Dev.*, 1998, **45**, 406-416; DOI: 10.1109/16.658674

[99] D. Veksler, G. Bersuker, A. Koudymov, and M. Liehr, "Analysis of Charge-Pumping Data for Identification of Dielectric Defects," *IEEE Trans. Elect. Dev.*, 2013, **60**, 1514 – 1522; DOI: 10.1109/TED.2013.2249070

[100] T.-M. Tsai, K.-C. Chang, T.-C. Chang, G.-W. Chang, Y.-E. Syu, Y.-T. Su, G.-R. Liu, K.-H. Liao, M.-C. Chen, H.-C. Huang, Y.-H. Tai, D.-S. Gan, C. Ye, H. Wang, and S. M. Sze, "Origin of Hopping Conduction in Sn-Doped Silicon Oxide RRAM With Supercritical CO_2 Fluid Treatment," *IEEE Elect. Dev. Lett*., 2012, **33**, 1693-1695; DOI: 10.1109/LED.2012.2217932

[101] V. Mikhelashvili and G. Eisenstein, "Effects of annealing conditions on optical and electrical characteristics of titanium dioxide films deposited by electron beam evaporation," *J. Appl. Phys*., 2001, **89**, 3256-3269; DOI: 10.1063/1.1349860

[102] D. Ielmini, D. Sharma, S. Lavizzari, and A. L. Lacaita, "Reliability Impact of Chalcogenide-Structure Relaxation in Phase-Change Memory (PCM) Cells—Part I: Experimental Study," *IEEE Trans. Electron Devices*, 2009, **56**, 1070-1077; DOI: 10.1109/TED.2009.2016397

[103] S. Lavizzari, D. Ielmini, D. Sharma, and A. L. Lacaita, "Reliability Impact of Chalcogenide-Structure Relaxation in Phase-Change Memory (PCM) Cells— Part II: Physics-Based Modeling," *IEEE Trans. Electron Devices*, 2009, **56**, 1078-1085; DOI: 10.1109/TED.2009.2016398

[104] A. Calderoni, M. Ferro, D. Ielmini, and P. Fantini, "A Unified Hopping Model for Subthreshold Current of Phase-Change Memories in Amorphous State," *IEEE Elect. Dev. Lett*., 2010, **31**, 1023-1025; DOI: 10.1109/LED.2010.2052016

[105] Y. Okuyama, S. Kamohara, Y. Manabe, K. Okuyama, K. Kubota, T. Kobayashi, and K. Kimura, "Monte Carlo Simulation of Stress-Induced Leakage Current by Hopping," *IEEE International Electron Devices Meeting (IEDM),* 1998, 905-908

[106] S. D. Ganichev, E. Ziemann, W. Prettl, I. N. Yassievich, A. A. Istratov and E. R. Weber, "Distinction between the Poole-Frenkel and tunneling models of electric-field-stimulated carrier emission from deep levels in semiconductors," *Phys. Rev. B*, 2000, **61**, 361 – 365

[107] D. Garetto, Y. M. Randriamihaja, D. Rideau, A. Zaka, A. Schmid, Y. Leblebici, and H. Jaouen, "Modeling Stressed MOS Oxides Using a Multiphonon-Assisted Quantum Approach—Part II: Transient Effects," *IEEE Transactions on Electron Devices*, 2012, **59**, 621 – 630; DOI: 10.1109/TED.2011.2181389

[108] Y.-L. Wu and S.-T. Lin, "Two-Trap-Assisted Tunneling Model for Post-Breakdown I−V Characteristics in Ultrathin Silicon Dioxide," *IEEE Transactions on Device and Materials Reliability*, 2006, **6**, 75 – 80; DOI: 10.1109/TDMR.2006.870351

[109] A. Mehonic, S. Cueff, M. Wojdak, S. Hudziak, C. Labbe, R. Rizk and A. J. Kenyon, "Electrically tailored resistance switching in silicon oxide," *Nanotechnology*, 2012, **23**, 455201-1 – 455201-9; DOI: 10.1088/0957-4484/23/45/455201

[110] Y. F. Chang, P. Y. Chen, B. Fowler, Y. T. Chen, F. Xue, Y. Wang, F. Zhou, and J. C. Lee, "Study of ambient effect in active SiO_x-based resistive switching memory," *2013 International Symposium on VLSI Technology, Systems and Applications (VLSI-TSA)*, 2013, 1-2; DOI: 10.1109/VLSI-TSA.2013.6545589

Figure Captions:

Figure 1. Cross-section schematics of three RM device architectures used to investigate electroforming and RS in amorphous SiO_2 materials: (a) MIS-edge device with exposed SiO_2 sidewall; (b) TiW MIM crossbar with exposed sidewall; (c) Passivated MIS-bulk device with continuous SiO_2 layer; (d) TEM cross section of MIS-edge device; (e) SEM top-down (upper) and cross-section (lower) images of TiW MIM device; and (f) SEM cross-section of passivated MIS-bulk device.

Figure 2. Electroforming results for devices having a sidewall edge. (a) Electroforming sweeps for SiO_2 materials deposited using: (1) thermal oxidation (30 nm); (2) e-beam evaporation (47 nm); (3) PECVD (60 nm); and (4) e-beam (51 nm) with 5-minute, 500 °C RTA in 4% D_2/N_2. (b) Average electroforming voltage V_{EF} versus PDA temperature and ambient for 5-minute RTA of ten Al / 50 nm e-beam SiO_2 / N^+Si devices at each condition with ± 3 V standard deviation bars.

Figure 3. Bulk device electroforming *I-V* plot for a TaN/e-beam oxide (51 nm)/N+Si MIS-bulk device with 5-minute, 500 °C RTA in 4% D_2/N_2. Dashed line marks V_{EF} = 13.4 V.

Figure 4. Fraction of CFs remaining intact after dilute HF etch to various depths.

Figure 5. MIM device states in vacuum: (a) six different devices measured at 0.2 V after a series of sweeps to 2 V; (b) four devices with current measured periodically at 2 V throughout a 1000-second stress time as a function of stress voltage V_{Stress}; and (c) current measured at 0.2 V during 100 °C thermal stress for devices programed to the LRS and several intermediate states using different stop voltage (SV).

Figure 6. Switching *I-V* response for: (a) MIM sidewall device with TiW electrodes, 60 nm PECVD SiO_2, V_S = 2.6 V, V_R = 4.0 V, switching in vacuum; and (b) MIS bulk device with 51 nm e-beam SiO_2, Pd/Si electrodes, SU8 passivation, V_S = 2.53 V, V_R = 4.97 V, switching in 1 atm air.

Figure 7. Effects of varying RESET Stop Voltage showing: (a) SET voltage V_S (circles), HRS Resistance (squares) and LRS Resistance (triangles) versus Stop Voltage; and (b) V_S versus HRS Resistance, R_{HRS}. In (a), dashed line is linear fit to V_S data, solid line is exponential fit to HRS Resistance data, and dotted line is polynomial fit to LRS Resistance data. In (b), dashed line is logarithmic fit to V_S data.

Figure 8. (a) First 8V sweeps in 1 atm ambient (after vacuum electroforming and cycling), averaged for 7 LRS MIM devices in 20% O_2/N_2, 7 HRS devices in 20% O_2/N_2, 7 LRS devices in air, and 7 HRS devices in air. (b) Averaged *I-V* response in vacuum after operating attempts in 1 atm ambient. The average of 14 first 8 V sweeps under vacuum for devices previously cycled in O_2/N_2 indicate recovery of RS at 4.6 ± 0.8 V (square symbols). Eighty-four 8 V vacuum sweeps were averaged for the devices cycled in air without recovery (dashed line). Devices cycled in air recovered after forward/reverse sweeps to an average value of 9.5 ± 0.8 V with one device requiring 11 V (solid line). (c) Average of 3 vacuum RS cycles from each of the 14 devices exposed to 1 atm O_2/N_2 (42 curves, solid line) and air (42 curves, dashed line) after vacuum recovery, indicating a characteristic unipolar response.

Figure 9. Normalized noise power spectral density measurements for 5 TaN MIS devices set to the LRS and 5 devices set to the HRS. Green line is $1/f$ trend and red line is $1/f^2$ trend.

Figure 10. Schematic representation of defects near SiO_2 sidewall illustrating: (a) oxygen reduction and ion drift mechanisms that may occur during electroforming; (b) the results of oxygen reduction and ion drift mechanisms possibly leading to the defects responsible for RS; (c) cross-section view of sidewall region after forming CF with ~ 4 nm lateral depth into SiO_2 sidewall; (d) front-on view of sidewall in LRS where all defects in switching region l_{SW} are in their ON state; and (e) front-on view of sidewall in HRS where defects within l_{GAP} are in their OFF state. Dashed lines mark the switching region with length l_{SW}. Illustrated gap length is $l_{GAP} \sim l_{SW}/2$.

Figure 11. Some of the known defects in SiO_2. Switching charge states are labeled: (+) positive, (0) neutral and (–) negative.

Figure 12. RS model defect transitions. ON state (top) contains Si-H-Si and Si_2=O-H_3O^+. Electron injection into H_3O^+ releases a proton (right-side intermediate state). Electrochemical reaction between the proton (H^+) and Si-H-Si forms $(SiH)_2$ and water absorption forms $(SiOH)_2$ to switch the complex OFF (bottom). Charging $(SiH)_2$ positive leads to H^+ desorption from SiH (left-side intermediate state). Proton uptake by absorbed water forms Si_2=O-H_3O^+ and switches the complex ON (top).

Figure 13. Energy band diagrams for: (a) LRS assuming R_S = 50 Ω and I_R = 2.63 mA, showing theoretical bandgaps of Si-H-Si and SiH+SiSi(5), 2.5 eV offset of H_3O^+ energy level from Si-H-Si conduction band, switching region of length l_{SW} and F-N tunneling RESET transition; and (b) HRS showing theoretical bandgap of $(SiH)_2$ defect within gap region of length l_{GAP} and TAT SET transition. Both diagrams are drawn for applied voltage V_A = 2.63 V. The LRS and HRS electron energy barriers are ϕ_{LRS} and ϕ_{HRS}, respectively.

Figure 14. (a) Average measured current I_{MEAS} of ten 8V RESET sweeps versus adjusted voltage V_{ADJ}. The LRS was programed using a forward/reverse voltage sweep to 3.5 V. The applied voltage V_A was adjusted to account for the voltage drop across the series resistance of R_S = 235 Ω using $V_{ADJ} = V_A - I_{MEAS} \times R_S$. The I_{MEAS} data are fit to the hopping formula from 0 – 1.5 V to obtain I_{HOP} (dashed line). A linear fit to the I_{MEAS} data in the voltage range from 2.2 to 2.7 V (dash-dot line) estimates the overshoot threshold voltage V_{TH} = 1.62 V. The TAT current component I_{TAT} (dotted line) in (a) is obtained from the linear fit to a plot of $\ln(I_{MEAS} - I_{HOP})$ versus V_{ADJ}^2 shown in (b). The linear fit to a plot of $\ln[(I_{MEAS} - I_{HOP})/V_{ADJ}^2]$ versus $1/V_{ADJ}^2$ in (b) confirms that F-N tunneling also fits the I_{MEAS} data in the overshoot region. The solid line in (a) shows the LRS current model: $I_{MODEL} = I_{HOP} + I_{TAT}$.

Table Headings:

Table I. Summary of experiment exposing MIM devices to 1 atm of O_2/N_2 or air.

Table II. Defect positive (+), neutral (0) and negative (–) switching charge-states, unoccupied switching charge-state energy levels (E_C), thermodynamic energy levels (E_{TH}), occupied switching charge-state energy levels (E_V) and effective bandgap energies (ΔE_G) referenced to the Si midgap energy in units of eV [43].